A robust evaluation of TDP-43, poly GP, cellular pathology and behavior in a AAV- C9ORF72 (G 4 C 2) 66 mouse model

Emily G. Thompson

Johns Hopkins University School of Medicine

Olivia Spead

Johns Hopkins University School of Medicine

S. Can Akerman

Johns Hopkins University School of Medicine

Carrie Curcio

Glaxo Smith Kline Research and Development

Benjamin L. Zaepfel

Johns Hopkins University School of Medicine

Erica R. Kent

Johns Hopkins University School of Medicine

Thomas Philips

Johns Hopkins University School of Medicine

Balaji G. Vijayakumar

Johns Hopkins University School of Medicine

Anna Zacco

Glaxo Smith Kline Research and Development

Weibo Zhou

Johns Hopkins University School of Medicine

Guhan Nagappan

Glaxo Smith Kline Research and Development

Jeffrey D. Rothstein

`jrothstein@jhmi.edu`

Johns Hopkins University School of Medicine

Research Article

Additional Declarations: No competing interests reported.

Abstract

The G_4C_2 hexanucleotide repeat expansion in *C9ORF72* is the major genetic cause of both amyotrophic lateral sclerosis (ALS) and frontotemporal dementia (FTD) (C9-ALS/FTD). Despite considerable efforts, the development of mouse models of C9-ALS/FTD useful for therapeutic development has proven challenging due to the intricate interplay of genetic and molecular factors underlying this neurodegenerative disorder, in addition to species differences. This study presents a robust investigation of the cellular pathophysiology and behavioral outcomes in a previously described AAV mouse model of C9-ALS expressing 66 G_4C_2 hexanucleotide repeats. The model displays key molecular ALS pathological markers including RNA foci, dipeptide repeat (DPR) protein aggregation, p62 positive stress granule formation as well as mild gliosis. However, the AAV-$(G_4C_2)_{66}$ mouse model in this study has marginal neurodegeneration with negligible neuronal loss, or clinical deficits. Human C9orf72 is typically associated with altered TAR DNA-binding protein (TDP-43) function, yet studies of this rodent model revealed no significant evidence of TDP-43 dysfunction. While our findings indicate and support that this is a highly valuable robust and pharmacologically tractable model for investigating the molecular mechanisms and cellular consequences of (G_4C_2) repeat driven DPR pathology, it is not suitable for investigating the development of disease- associated TDP-43 dysfunction or clinical impairment. Our findings underscore the complexity of ALS pathogenesis involving genetic mutations and protein dysregulation and highlight the need for more comprehensive model systems that reliably replicate the multifaceted cellular and behavioral aspects of C9-ALS.

Introduction

Amyotrophic lateral sclerosis (ALS) is a progressive and ultimately fatal neurodegenerative disease that affects upper and lower motor neurons in the cerebral cortex, brainstem and spinal cord. The degeneration of motor neurons leads to muscle denervation and atrophy with paralysis and death three to five years after disease onset due to respiratory insufficiency [41, 81]. While most ALS cases have no known genetic cause, an intronic GGGGCC hexanucleotide repeat expansion (HRE) in the *C9ORF72* gene is responsible for the majority of familial ALS (fALS) and a subset of sporadic ALS (sALS) [17, 67]. In a healthy individual, the intronic G_4C_2 repeat length can range from 2–30 repeats. However, in patients with C9-ALS, this region may contain hundreds to thousands of repeats [7, 17, 31, 47, 67, 71].

The mechanism by which this G_4C_2 expansion leads to cellular dysfunction is not yet fully elucidated, however there are several hypotheses currently under investigation. Patients with C9-ALS may show decreased coding C9ORF72 mRNA and protein expression, resulting in loss of function of the endogenous C9orf72 protein [16, 21, 29, 84]. In addition, the repeat expansion causes a gain of toxic function in which the intronic repeat mRNA is transcribed and forms nuclear and cytoplasmic mRNA foci [16, 18, 23]. These cytoplasmic repeat mRNAs can also undergo repeat-associated non-ATG-dependent (RAN) translation, forming aggregation-prone dipeptide repeat proteins (DPRs) [3, 38, 51, 56, 57]. Five different DPR protein species are produced from either sense or antisense transcripts of the HRE. Poly

Glycine-Alanine (polyGA), Glycine-Arginine (polyGR), and Glycine-Proline (polyGP) are produced from sense HRE transcripts, while polyGP, Proline-Alanine (polyPA), and Proline-Arginine (polyPR) are generated from antisense HRE transcripts. It is still unclear how or whether RNA foci themselves significantly contribute to cellular toxicity, but it is possible that the RNA foci structures sequester various RNA-binding proteins, leading to the loss of their function [12, 39] and the repeat RNA themselves may impair nucleocytoplasmic transport or the nuclear pore complex structure [14]. DPRs, particularly arginine-rich DPRs, have been implicated in several toxicity-inducing pathways including DNA damage and oxidative stress [44], ER Stress [88], impairment of protein translation and stress granule dynamics [27, 85], and disruption of nucleocytoplasmic transport [20, 32, 73]. Interestingly, in ALS patient brains, DPR accumulations are found in both degenerating and non-degenerating cell types, indicating a more complicated role for DPR inclusions in neuronal toxicity [82].

TAR DNA-binding protein-43 (TDP-43) is a nuclear DNA/RNA-binding protein involved in a several cellular functions including transcriptional as well as post-transcriptional regulation such as RNA splicing, mRNA transport, and translational repression [76]. An overwhelming majority of ALS cases display TDP-43 disruption, characterized by both the nuclear loss of the endogenous protein as well as cytoplasmic inclusions of hyperphosphorylated-TDP-43 [2, 58, 74]. TDP-43 dysfunction due to loss-of-nuclear function and gain-of-cytoplasmic functions are believed to be responsible for TDP-43 driven neurodegeneration [6, 36, 46, 49, 76]. Additionally, TDP-43 aggregates are known to alter many cellular functions through the sequestration of other proteins. For example, in artificial overexpression systems, TDP-43 aggregates sequester nuclear pore complexes and nucleocytoplasmic transport components, altering nuclear import and export [11]. TDP-43 aggregates co-localize with stress granule components, altering their dynamics and possibly increasing cell sensitivity to prolonged stressors [34, 48]. These aggregates are also known to inhibit proteasome function and autophagy which promotes the accumulation of toxic misfolded protein in the cell [22, 53, 58, 77]. It should be noted that recent studies suggest artificial TDP-43 overexpression does not mimic the known changes of TPP-43 loss of function, typically seen in actual human tissue [8].TDP-43 also plays a role in the intracellular and axonal transport of mRNA granules and this function is lost when it is aggregated [1, 19, 72]. However, the actual abundance of TDP-43 aggregate is in reality quite low in human autopsy tissue, while nuclear loss is far more common, suggesting that the loss of function may be the dominant toxicity pathway. While the underlying pathogenic mechanisms mediated by TDP-43 are diverse, it is clear that TDP-43 mislocalization and aggregation lead to neuronal death in C9-ALS [4, 5, 28, 78].

Historically, the use of mouse models has driven *in vivo* efforts to understand disease etiology, mechanisms, and therapeutic opportunities. As with various other neurodegenerative diseases, there has been a concerted effort to create a reliable mouse model for C9-ALS. This has resulted in a plethora of individual models, each with advantages and shortcomings. Collectively, these models have improved our understanding of aspects of C9-ALS pathobiology, such as the role of individual DPRs in pathophysiology. For example, ubiquitous expression of a 50-repeat length polyGR peptide (GR50) resulted in sex-specific neuronal loss and behavioral deficits [83]. Hao and colleagues generated a loxP-Cre line to drive expression of a 28-repeat length polyPR peptide (PR28) in Thy1-neurons, resulting in

gliosis, synaptic dysfunction, and motor abnormalities [26]. Similarly, when a 50-repeat length polyGA peptide (GA50) was expressed in the mouse brain using an adeno-associated virus (AAV), mice display neuronal loss throughout the brain and deficits in behavior including memory and motor coordination [89]. While the above-mentioned models sought to express specific DPRs in an attempt to understand specific DPR polypeptide overexpression biology, several models have also been developed to express the G_4C_2 HRE at varying repeat lengths, perhaps more closely mimicking authentic human disease. One such model expresses 36-G_4C_2 repeats under inducible control with varying phenotypes depending on the promoter [69]. Several groups have used a bacterial artificial chromosome (BAC) DNA clone containing varying lengths of the human *C9ORF72* gene, including G_4C_2 repeats ranging from 100–1000, to generate transgenic mice in hopes of modeling "authentic" ALS [30, 42, 60, 61]. Varying degrees of cellular pathology, neuronal loss, and motor phenotypes have been observed in these mouse models. The high variability of expression levels both within and between lines has raised some questions as to the validity of this model. Oftentimes, even replicated studies have had inconsistent results [55, 59].

In addition to germline transgenic models, a mouse model that utilized viral transduction of 66 G_4C_2 repeats (($G_4C_2)_{66}$) directly into the CNS of neonatal mice was developed [10, 69]. Upon transduction, neurons express the $(G_4C_2)_{66}$ RNA which is translated to produce the three sense-strand-specific DPRs (polyGA, GP, and GR). These mice were found to display many of the pathologies seen in ALS/FTD patients including RNA foci, DPR pathology, pTDP-43 inclusions, and motor deficits as tested by rotarod [10]. It is not yet known whether these exhibit nuclear clearance or loss of function of TDP-43, both typical in authentic human C9-ALS. Moreover, a robust characterization of the AAV-$(G_4C_2)_{66}$ mouse model, including comprehensive assessment correlating the biochemical pathology, cellular dysfunction, and behavioral outcomes associated with this model was needed. Therefore, in this study we sought to make this assessment using a robust study design including randomization of animals at multiple levels, blinding until completion of statistical analysis, and a sample size based on power analysis with two primaryendpoints (rotarod and brain polyGP).

Methods

Animals

C57BL/6J were purchased from Jackson Laboratories (Strain #000664) at 4–8 weeks of age. At 6–9 weeks of age breeding pairs were established to produce pups for all subsequent experiments. Both male and female mice were used throughout the study and randomly allocated to each of the experimental groups. Mice were housed in a constant 14-hour light/ 10-hour dark cycle and allowed access to food and water *ad libitum*. All animal procedures were carried out in compliance with animal protocols approved by the Animal Use Committee at the Johns Hopkins University School of Medicine (JHUSOM) as well as in accordance with the GSK Policy on the Care, Welfare and Treatment of Laboratory Animals. This study was reviewed by the Institutional Animal Care and Use Committee at GSK, and at JHUSOM where the work was performed.

Generation of AAV2/9-(GC) and AAV2/9-(GC) vectors

The AAV2/9-$(G_4C_2)_2$ and AAV2/9-$(G_4C_2)_{66}$ viruses were provided by Dr. Leonard Petrucelli at Mayo Clinic Jacksonville. The viruses were prepared as previously described [10, 75]. Following generation, the genomic titer of each virus was determined by qPCR and the AAVs were diluted with sterile phosphate buffered saline (PBS) and stored at -80°C until use.

Randomization, Blinding, and Power Analysis

This study was powered based on rotarod performance and brain polyGP levels as the primary endpoints, motivated by a review of the raw data from the previously described study [10]. The pooled standard deviation of latency-to-fall was estimated as 24.87 seconds with 20 degrees of freedom. In order to obtain a conservative power estimate and mitigate the risk of underpowering the current study, the upper 80% confidence limit of 29.13 seconds was used to calculate the statistical power. The power analysis was based on an ANOVA model accounting for sex and experimental group as factors. With a target sample size of n = 20 per experimental group (n = 10 per sex per group), this study had 80% statistical power to find statistically significant differences in rotarod response between groups as small as 23.3 seconds.

Similarly, an analogous power analysis was conducted using polyGP data [24], which yielded a standard deviation estimate of 1.66 log-2 cells/μm^2 with 8 degrees of freedom. Using the upper 80% confidence limit (2.2 log-2 units) of this estimate, this study had 80% statistical power to find statistically significant differences in quantification of polyGP as small as 1.76 log-2 units, or a 3.39-fold increase between groups in cells/μm^2.

Within the first 24 hours of life (postnatal day 0–1), pups were randomized to receive either AAV2/9-$(G_4C_2)_{66}$ injection, AAV2/9-$(G_4C_2)_2$ injection, or no injection, littermate matched at a ratio of 1-1-1, respectively. Upon weaning, animals were separated by sex and randomized to cages. Animals with the same AAV-$(G_4C_2)_x$ repeat injection were housed in the same cage. Upon in-life study completion, ex-vivo study samples were randomized among plates for the MSD assay.

Investigators who were monitoring the behavior performance and in-life care were blinded to the experimental groups. Body weight collection throughout the study and end-of-life tissue collection were not blinded. Ex-vivo samples were labeled with only mouse IDs without experimental group information.

Neonatal Viral Injections

AAV viral aliquots were thawed on ice and spun down in a centrifuge at 4°C. In a sterile hood, viruses were diluted to 1.5×10^{10} viral genomes/μL (vg/μL) with sterile PBS and were stored on ice until time of injection. Intracerebroventricular (ICV) injections of AAV were performed on C57BL/6J postnatal day 0

(P0) pups. AAV dilutions were prepared on the day of injections. Pups underwent cryoanesthesia on ice for approximately 3 minutes or until pups exhibited no movement. A 32-gauge needle (Hamilton; Small RN 32 gauge, 0.5 inch needle, point style 4) attached to a 10 µL syringe (Hamilton, Model 701 RN) was inserted approximately two fifths of the distance between the lambda and each eye at a 30° angle from the surface of the head and was held at a depth of about 2 mm. 2 µL of virus was manually injected into each cerebral ventricle and the needle was held in place for an additional 5 seconds after each injection to prevent backflow. After injections, pups were placed on a heating pad until fully recovered and then returned to their home cages with the dam. Any pups with back flow from the injection were excluded from the study.

Intracerebroventricular (ICV) anti-sense oligonucleotide (ASO) injection

ASO Preparation

A C9ORF72-ASO was prepared by Integrated DNA Technologies with the following sequence: 5'-mC*mC*mG* mG*mC*C* C*C*G* G*C*C* C*C*G* mG*mC*mC* mC*mC -3' with standard desalting, Na^+ Salt Exchange, and analytical RP-HPLC. Additionally, to reduce adverse *in vivo* effects from Ca^{2+} chelation, we pre-saturated ASO calcium binding sites by transferring the ASO to a 3 kDa-cutoff ultrafiltration cartridge (Amicon) and washed twice with 10 mM $CaCl_2$ followed by water, and finally with PBS [54]. All spins were performed at 4°C. The ASO was then resuspended with PBS, concentration determined with NanoDrop and diluted to 50 ng/µL with PBS for ICV injection.

ICV injection

Delivery of the above described C9-ASO was performed in mice at 90 dpi (days post AAV injection) with stereotactic ICV injection. After isoflurane anesthesia, slow-release Buprenorphine was injected subcutaneously (1 mg/kg) prior to the surgery. While maintaininganesthesia via nose cone, the animal's skull was immobilized on a Stoelting stereotaxic frame. Hair was removed from the scalp with a chemical depilatory cream (Nair) and sterilized with topical disinfectant (Betadine) and 70% ethanol. Using sterile instruments and gloves, a mid-sagittal longitudinal incision of approximately 0.5 cm was made on the scalp to expose the skull and the subcutaneous tissue and periosteum were scraped from the skull with a sterile cotton tipped applicator. At the following coordinates: 0.0 mm anterior to bregma and 1.0 mm to the right lateral, a small burr hole was drilled through the skull with a hand drill attached to a micromanipulator to expose the brain. A Hamilton syringe (Hamilton 7635-01) was filled with either PBS or C9-ASO at 50 ng/µL and attached to a microinjection pump (World Precision Instruments Micro 4) on a stereotactic arm. After alignment of the syringe needle at 90° to the burr hole and surface of the brain, the syringe was slowly lowered 1.9 mm into the brain. 10µL of the loaded solution was then injected with the microinjection pump at a rate of 2 µL/min, followed by a 5-minute wait period. The

syringe was then slowly removed, and the incision site was closed with 5 – 0 polyglactin 910 (Vicryl) absorbable suture. Antibiotic ointment (Fisher Scientific 19-090-845) was applied to the wound and the animal was allowed to fully recover from theanesthesia on a warmed heating blanket. Carprofen (Rimadyl) at 0.05 mg/mL wasadministered in drinking water for seven days post-surgery to manage pain.

Body Weight measurements

Body weight (g) was measured every two weeks for all animals starting at 90 dpi until the conclusion of the study.

Behavioral Assays

Mice underwent several behavior tests, including rotarod, grip strength, catwalk, and open-field assessments, at 90 and/or 180 dpi. One week before behavioral assessments, mice were habituated to the equipment used for behavior testing as well as to those running the behavior tests. Animals were placed on the equipment and allowed to explore for two minutes each. Scientists running the tests also gently handled the mice for 2–3 minutes, placing their hand in the cage and allowing the mice to explore, to decrease the stress in the mice prior to behavioral testing.

Rotarod

Motor coordination and learning was assessed using an automated rotarod system (Columbus Instruments, Rotamex-5, 0254–8000). Mice were gently placed on a rod that accelerated from 4 to 40 rpm at a rate of 1.2 rpm every ten seconds. Four trials were run for each mouse with at least 20 minutes of rest in between. The latency to fall time was recorded for each trial when the mouse fell from the rod, triggering the sensor to automatically stop the timer. When the mouse fell and clung to the rod or rolled around the rod three consecutive times, the mouse was manually removed from the rod and the corresponding time was recorded as the time of the fall.

Grip Strength

The strength of the fore- and hindlimbs of each mouse was measured using a T-bar with an attached meter (Chatillon 2 LBF Ametek Force Gauge) to measure the peak force exerted from each mouse. Each mouse was held by the tail and lowered gently until the front paws were gripping overhand on the T-bar. The mouse was gently pulled back and the force exerted on the bar just before the mouse lost its grip is recorded. For hindlimb assessment, mice were held by the tail and gripped a metal rod with their forelimbs. The mice were lowered until their back paws gripped the T-bar. They were gently pulled back and the maximum force before losing grip was recorded. Each mouse was tested four times for both fore- and hindlimbs.

Catwalk

Gait analysis was assessed using the Catwalk XT Automated Gait Analysis System (Noldus Technology, Software Version 10.6.608). Mice walked within a corridor across an illuminated glass platform while a camera recorded underneath. Walking from one end to the other was recorded as one trial and each mouse ran five consecutive trials. From the recordings, each individual pawprint was digitized and labeled into a discrete number of pixels with a range of brightness. This information was quantified using CatWalk (ver. 10.6.608) software to generate numerous parameters of quantitative and qualitative assessment of individual pawprints and gait.

Open field

The SDI (San Diego Instruments, San Diego, CA, USA) open field apparatus consisted of a plexiglass square box, 40.6 cm (W) x 40.6 cm (D) x 38.1 cm (L), with side mounted photobeams at 7.6 cm above the floor to measure rearing. All surfaces within the box were thoroughly cleaned with Vimoba disinfectant prior to testing each animal. Mice were placed in the center of the box and allowed to explore the area for 15 minutes. All movements were recorded and analyzed with the Photobeam Activity Systems Data Reporter software (SDI), and the following parameters were measured: total distance traveled, average speed, mobile time, and distance traveled in center zone (20 cm x 20 cm) vs. total distance traveled.

Statistical Analysis: Behavioral Assays

Rotarod data was analyzed using a two-way ANOVA with timepoint (90 dpi, 180 dpi) and experimental group as factors, controlling for repeated measures on mice. Grip strength at 90 dpi and open-field locomotion activity at 180 dpi were each analyzed using a one-way ANOVA with experimental group as a factor. Body weight was analyzed separately for males and females with a two-way repeated-measures ANOVA with timepoint and experimental group as factors. All ANOVAs were performed in Graphpad Prism (ver. 9.4.1). Overall family-wise error rate was controlled in all post-hoc pairwise comparisons for all assays using the Tukey-Kramer multiple comparison test [37, 79] unless otherwise noted.

The catwalk data at 90 dpi and 180 dpi was analyzed separately at each timepoint, using a linear mixed-effects model to account for correlation among 12 parameters (base of support, phase dispersion, stride length, body speed, cadence, number of steps, run speed, swing speed, print area, stand time, step cycle, and swing time). This no-intercept model used the interaction of experimental group and parameter as fixed effects, in order to obtain the group effect for each parameter; it also used a random intercept for each animal and parameter-specific residual variance estimates. Post-hoc least-squares means were compared among groups within parameter to assess differences in experimental groups. Multiplicity among comparisons for all parameter readouts was controlled using the Tukey-Kramer multiple comparison test. No statistically significant differences were found between any two experimental groups in any of the parameters; three parameters (step number, cadence, run speed) are displayed in Fig. 7D. The catwalk analysis was performed using SAS (ver. 9.4).

Cerebrospinal Fluid (CSF), Plasma, and Tissue collection

CSF

The mouse was anesthetized with an I.P. injection of 100 mg/kg ketamine-2.5 mg/kg acepromazine-10 mg/kg xylazine. When the animal was no longer responsive to toe pinch the neck musculature was retracted to expose the cisterna magna. A cauterizing iron was utilized to stop any bleeding from the musculature and a cotton applicator soaked in PBS was used to remove any blood. A 25-gauge needle was then used to puncture the cisterna magna dura and a 20 μL pipette was used to collect the CSF (approximately 5–20 μL). Any blood contaminated CSF samples were centrifuged at 3000 x g and the supernatant was transferred to a new tube. All samples were stored in low-binding microcentrifuge tubes (Eppendorf 0030108442) on dry ice prior to storage at -80°C.

Plasma

After CSF collection, the chest cavity of the animal was opened to provide access to the heart. A 20-gauge needle was attached to a 3 mL syringe and used to puncture the left ventricle of the heart. Negative pressure was slowly applied via the syringe for blood collection. The blood was centrifuged at 3000 x g at 4°C for 15 minutes. The plasma supernatant was aliquoted at 60 μL per microcentrifuge tube and snap frozen. All samples were stored at -80°C.

Brain

The anesthetized mouse was transcardially perfused with ice-cold PBS containing 10 U/mL heparin (Sigma-Aldrich H3149) for approximately 5 minutes. Subsequently, the brain was removed, and the right hemisphere was snap frozen in a microcentrifuge tube. The left hemisphere was either snap frozen or put into a microcentrifuge tube containing 4% paraformaldehyde (PFA) in PBS overnight at 4°C and then moved into PBS containing 0.1% sodium azide for long store storage. 4% PFA fixed brain tissues were transferred to 10% sucrose solution overnight at 4°C. The brain tissue was then processed by Johns Hopkins reference histology facility for paraffin embedding in sagittal orientation. Paraffin blocks were then cut into 5 μm sections using a microtome.

Spinal Cord

The spinal cord was extracted by hydraulic extrusion, as previously described [68]. The spinal column was dissected, cutting distally to the pelvic bone and proximally of the shoulders, and then trimmed until the spinal cord was visible at both ends. A 20-gauge needle connected to a 5 mL syringe filled with PBS was inserted into the distal end of the spinal column, ensuring the needle was stabilized within the column. Making sure the spinal column was straightened as much as possible, steady pressure was applied to extrude the spinal cord into a petri dish filled with cold PBS. The spinal cord was cut into Cervical, Thoracic, and Lumbar sections. The Thoracic sections were snap frozen and the Cervical and Lumbar sections were put into microcentrifuge tubes containing 4% paraformaldehyde in PBS overnight at 4°C and then moved into PBS containing 0.1% sodium azide for long store storage.

Brain and Spinal Cord Homogenization

Frozen whole brain hemispheres and thoracic spinal cord samples were quickly transferred to a Lysing Matrix D tube (MP Biomedicals 116913050) and ice-cold Homogenization Buffer (Tris-EDTA buffer, pH 8.0 [ThermoFisher Scientific AM9858] and 1X Protease [Millipore 539131] and Phosphatase Inhibitor Cocktail [Bimake B15002]) was added. The sample was homogenized with an MPbio FastPrep machine for 1 minute. After homogenization the tube was spun at 1500 x g for 2 min. at 4°C to remove bubbles. Part of the homogenate was transferred to a tube containing Trizol (ThermoFisher Scientific 15596026) for subsequent RNA isolation, while the rest of the homogenate was transferred to a tube containing 2X Lysis Buffer (50 mM Tris pH 7.5 [Quality Biological 351-006-131], 250 mM NaCl [Quality Biological 351-036-101], 2% Triton X-100 [Sigma-Aldrich T9284], 4% SDS [ThermoFisher Scientific AM9820], 2X Protease [Millipore 539131] and Phosphatase Inhibitor Cocktail [Bimake B15002], and 2 mM PMSF [ThermoFisher Scientific 36978]) and vortexed briefly to mix. The lysate was incubated on ice for 10 min., after which the lysate was spun at 16,000 x g for 20 min. at 4°C. The supernatant was transferred to a fresh tube and stored at -80°C until further analysis.

Meso Scale Discovery (MSD) Assay

Sample Preparation

Brain and spinal cord lysate samples were thawed on ice and a BCA Protein Assay (ThermoFisher Scientific 23225) was performed per manufacturer's instructions to determine total protein concentration of the sample. Subsequently, samples were prepared at 1.0 µg/35µL homogenate buffer and stored at -80°C.

MSD Assay

Blocking buffer (Meso Scale Diagnostics R93AA-1) was prepared per manufacturer's instructions, added to the wells of an MSD Gold 96 Well Small Spot plate (Meso Scale Diagnostics L45SA1), and incubated overnight at 4°C. The plate was washed with PBST (0.05% Triton X-100 in PBS). A polyGP capture antibody (generated in [9]) was conjugated with biotin in house (ThermoFisher Scientific A39256), diluted to 0.375 µg/mL PBS, added to each well, and incubated with shaking at room temperature for 1 hour. The plate was then washed with PBST and poly-(GP)$_8$ peptide (CKK-PEG2-GPGPGPGPGPGPGPGP-amide; 21st Century Biochemicals) standards and brain hemisphere or spinal cord samples (1.0 µg/well), diluted in PBS, were added to the plate in triplicates. Incubation occurred for 3 hours at RT with shaking. Following PBST washes the sulfo-tagged polyGP detection antibody (polyGP antibody [9] conjugated in house with Meso Scale Diagnostics R31AA-1) was diluted 0.5 µg/mL to PBS and added to each well. The plate was incubated with shaking at RT for 1 hour. After washing with PBST, MSD Gold Read Buffer A (Meso Scale Diagnostics R92TG-2) was added to each well and the plate was read with the MESO QuickPlex SQ MSD machine. The polyGP signal value for each sample was then calculated with MSD Discovery Workbench 4.0 Analysis software and the average of each sample triplicate plotted.

RNA isolation, cDNA synthesis, and RT-qPCR

Total RNA from brain and spinal cord was isolated using the standard TriZol protocol followed by purification using the Direct-zol RNA Miniprep or Microprep kit (Zymo Research R2052). The concentration of RNA samples was determined using a NanoDrop One (Thermo Fisher Scientific). 1μg RNA was used for cDNA synthesis using the High Capacity cDNA Reverse Transcription Kit (Applied Biosystems 4368814). qRT-PCR reactions were performed using TaqMan Fast Advanced Master Mix and an Applied Biosystems StepOnePlus Real Time PCR machine (Applied Biosystems) using commercially available primer-probe Taqman sets (Thermo Fisher Scientific) with Taqman Fast Advanced Master Mix (ThermoFisher Scientific 4444557) or primers and PowerUp Sybr Green Master Mix (Applied Biosystems A25741). Table 1 contains a list of all Taqman probes and primers used within the study. 10–20 ng of cDNA was used for each reaction and mRNA abundance was measured relative to *Gapdh* mRNA.

Technical duplicates or triplicates were utilized within each qRT-PCR plate. A negative control (NTC) was used for each probe to ensure the absence of detected background signal. qRT-PCR results are reported as delta C_T values (target C_T value − endogenous control C_T value) or as Fold Change using the Comparative C_T method [43].

Table 1
List of qRT-PCR primers and probes

Probe/Primer target	Taqman/SYBR	Sequence (SYBR) or Assay ID (Taqman)
Aif1	Taqman	Mm00479862_g1
Gapdh	SYBR	[25] Forward: 5'-AGGTCGGTGTGAACGGATTTG-3' Reverse: 5'-TGTAGACCATGTAGTTGAGGTCA-3'
Gapdh	Taqman	Mm99999915_g1
Gfap	Taqman	Mm01253033_m1
Grm2	SYBR	Forward: 5'-GAGAGCCAGCAAGCGGGAAC-3' Reverse: 5'-GGAAAGGACAGACAGGAAGAG-3'
Oasl2	SYBR	Forward: 5'-GGACCAAGAAGTCAGGGTGA-3' Reverse:5'-GCAGCTTAAGAACAGAATCATGTCT-3'
Olfml3	Taqman	Mm00513567_m1
Rspo1	SYBR	Forward: 5'-GGATCAAGGGCAAGAGACAGAGG-3' Reverse: 5'-GCACTTGAGGCAACCGTTGAC-3'
Sort1(cryptic species)	SYBR	[87] Forward: 5'-AAATCCCAGGAGACAAATGC-3' Reverse: 5'-GAGCTGGATTCTGGGACAAG-3'
Tardbp	SYBR	[87] Forward: 5'-GGGGCAATCTGGTATATGTTG-3' Reverse: 5'-TGGACTGCTCTTTTCACTTTCA-3'
Tmem119	Taqman	Mm00525305_m1
Trem2	Taqman	Mm04209424_g1
Tsn	SYBR	[87] Forward: 5'-GGTCTTCCTGGCAGCATTTG-3' Reverse: 5'-TTGACAGACAGCCTCGATGC-3'
Unc13a	SYBR	Forward: 5'-GGAGTCATGTCTCTGCTGTGC-3' Reverse: 5'-CTTCACGTTCTGCACCTTCAGC-3'
WPRE	SYBR	Forward: 5'-TACAGCTCCTGGGCAACG-3'

Probe/Primer target	Taqman/SYBR	Sequence (SYBR) or Assay ID (Taqman)
		Reverse: 5'-CTTGTTCACCCTCAGCGAGT-3'

RNA Fluorescence In Situ Hybridization

Formalin-fixed paraffin-embedded (FFPE) sections were prepared for RNA Fluorescence *In Situ* Hybridization with RNAscope reagents (Advanced Cell Diagnostics) according to manufacturer's instructions. In brief, tissue sections were dried at 60°C for 1 hour and then deparaffinized in xylene and rehydrated through a series of ethanol solutions. Next endogenous peroxidase activity was blocked with RNAscope Hydrogen Peroxide solution for 10 minutes at room temperature. Following distilled water washes, antigen retrieval was performed with 1X Target Retrieval Reagent at 99°C in a steamer for 15 minutes. Slides were next exposed to 100% ethanol for 3 minutes and dried at room temperature. RNAscope Protease Plus solution was added to each section and incubated at 40°C for 30 minutes and washed with distilled water. A probe designed to detect the 5' and 3' UTR of the virally expressed RNA (Advanced Cell Diagnostics, RNAscope™ Probe-hC9orf72-BGH-PolyA-C1, 1240972-C1) was added and incubated at 40°C for 2 hours and subsequently the RNAscope Multiplex Fluorescence v2 assay reagents were used as directed. Lastly, sections were incubated with DAPI for 30 seconds at room temperature, mounted with ProLong Gold (ThermoFisher Scientific P36934), and dried overnight.

Immunofluorescence

FFPE sections were deparaffinized in xylene and rehydrated through a series of ethanol solutions. Antigen retrieval was performed in 10 mM sodium citrate buffer, pH 6.0 for 60 minutes in a steamer and then allowed to cool for 10 minutes. Following washing with deionized water and PBS, the tissue was permeabilized with 0.2% Triton X-100 in PBS for 10 minutes at room temperature. The sections were then washed with PBS with 0.05% Tween (PBST) and blocked with 10% Normal Goat serum containing 0.1 – 0.05% Tween for 1 hour at room temperature. Sections were immunostained with primary antibodies (refer to Table 2) diluted in blocking buffer overnight at 4°C and were subsequently washed with PBST (PBS with 0.05% Tween). Goat secondary antibodies diluted in blocking solution were incubated at room temperature for 1 hour. The sections were thoroughly washed with PBST and mounted on a coverslip with Prolong Gold with DAPI mounting solution (ThermoFisher Scientific P36931).

Immunohistochemistry

FFPE sections were deparaffinized in xylene and rehydrated through a series of ethanol solutions. Antigen retrieval was performed in either distilled water (for polyGP, GA, GR staining) or in 10 mM sodium citrate buffer, pH 6.0 (for p62 and NeuN stainings) for 30 minutes. Tissues were immunostained with the following primary antibodies poly(GP), poly(GR), poly(GA), SQSTM1/p62, and NeuN. DAKO Envision + HRP polymer kits (K4003 and K4001) were used and the reaction visualized using ImmPACT® VIP Substrate Kit (Vector Laboratories SK-4605). Sections were then counterstained with Hematoxylin QS Counterstain (Vector Laboratories H-3404-100) and mounted with Aqua-Poly/Mount (Polysciences

18606-20). Slides were either imaged as 20x magnification tiles or individual 63x magnification images using Zeiss Axio Imager.

Table 2
List of antibodies for tissue staining.

Target	Source	Catalog #	Use(s)	Dilution
GFAP	Abcam	Ab4674	IF	Brain: 1:1000
Iba1	Wako	019-19741	IF	Brain: 1:1000 Spinal Cord: 1:500
NeuN	EMD Millipore	MAB377	IHC	Brain: 1:1000 Spinal Cord: 1:500
polyGA	Dr. Leonard Petrucelli, Generated in [90]		IHC	1:50,000
polyGP	Generated in [9]		IHC	1:10,000
polyGR	EMD Millipore	ABN1361	IHC	1:5000
Ran GTPase	BD Bioscience	610341	IF	1:100
SQSTM1/p62	ABClonal	A11250	IHC	1:100
TDP-43	ProteinTech	10782-2-AP	IF	1:100

NfL and GFAP assessment

Neurofilament light chain (NfL) and GFAP from plasma and CSF samples were assessed using the Quanterix® Neuro 2-Plex B assay (Quanterix 103520). Following the manufacturer's instructions, samples were blinded and run-in duplicate, along with two quality controls (high-concentration and low-concentration quality control) on each plate per run using the Quanterix SR-X™Analyzer® platform version 1.1. Plasma samples (60 µl plasma into 180 µl of sample diluent) were run using a 4-fold dilution while CSF samples (2.5 µl into 247.5 µl of sample diluent) were run using a 100-fold dilution and results were compensated for the dilution factor. NfL and GFAP concentrations (pg/mL) were calculated using a standard curve (Four parameter logistic (4PL) curve) provided by Quanterix® (Lot 503560).

Results

The C9ORF72 $(G_4C_2)_{66}$ viral construct is expressed in brain and spinal cord

We utilized a previously generated [10, 75] adeno-associated viral vector (AAV2/9) to drive expression of either 2 (control) or 66 G_4C_2 repeats within the intronic region of the chromosome 9 open reading frame 72 (*C9ORF72*) gene. C57BL/6J postnatal day 0 (p0) pups were administered either AAV2/9-*C9ORF72* $(G_4C_2)_2$ or AAV2/9-*C9ORF72* $(G_4C_2)_{66}$ viral particles via intracerebroventricular (ICV) injection (**Supplemental Fig. 1A**). To assess the expression of the viral constructs within the CNS, specifically the brain and spinal cord, qRT-PCR was performed on isolated total RNA samples at 180 days following ICV injection (dpi). We observed viral expression in both the $(G_4C_2)_2$ and $(G_4C_2)_{66}$ groups but not the PBS injected (sham) group as expected in the tissues (Fig. 1A, 1C). Viral RNA was only detectable in the brain and spinal cord of 66R animals and not observed in sham or $(G_4C_2)_2$ animals (Fig. 1B, 1D). In the $(G_4C_2)_{66}$ animals, viral RNA was found across all layers of the cortex, with elevated expression in layers II and III. We also detected a significant burden of viral RNA within the hippocampus, highest in the Cornu Ammonis (CA) regions, and in the thalamus (Fig. 1B). Within the spinal cord, we observed the highest level of viral RNA in the ventral horn of cervical sections from $(G_4C_2)_{66}$ animals, while no rRNA were detectable in sham or $(G_4C_2)_2$ animals (Fig. 1D). We did not observe viral RNA in lumbar spinal cord sections from sham, $(G_4C_2)_{66}$, or $(G_4C_2)_{66}$ animals (Fig. 1D). In **Supplemental Fig. 1B**, we have illustrated the collective distribution of the viral RNA that we observed in the brain and spinal cord of $(G_4C_2)_{66}$ animals.

C9ORF72 $(G_4C_2)_{66}$ mice display DPR expression in the brain and spinal cord

The *C9ORF72* HRE associated DPR peptides are produced by RAN translation [3, 38, 51, 56] from sense and antisense RNA. When we examined the tissue homogenates b y polyGP MSD, only $(G_4C_2)_{66}$ mice had a robust polyGP signal in both the brain and spinal cord (Fig. 2A). Importantly, the significant increase in polyGP signal detected in the brain of $(G_4C_2)_{66}$ mice was completely abolished with the delivery of a *C9ORF72* anti-sense oligonucleotide (C9-ASO) at 90 dpi via intracerebroventricular (ICV) injection, with no statistical difference found between the sham and $(G_4C_2)_{66}$ + C9-ASO groups in the brain (Fig. 2A). We also measured polyGP signal in thoracic spinal cord samples and found a significant increase in polyGP signal in the $(G_4C_2)_{66}$ mice (Fig. 2A). We observed approximately 10-fold less polyGP signal in spinal cord compared to brain polyGP signal in $(G_4C_2)_{66}$ animals—indicative of a greater polyGP burden in the brain than the spinal cord of $(G_4C_2)_{66}$ animals (Fig. 2A)—consistent with the reduced viral loads observed (Fig. 1C). Additionally, to gain insight into the expression and location of polyGP, polyGR, and polyGA species *in situ*, we performed immunohistochemistry on brain and spinal cord tissues. In the $(G_4C_2)_{66}$ transduced animals we observed robust polyGP signal within the nucleus of cells within the cortex, thalamus, and hippocampus, but not in $(G_4C_2)_2$ and sham animals (Fig. 2B-C, **Supplemental Fig. 2A-B**). For both polyGR and polyGA we observed smaller, aggregates perinuclear or within the nucleus of cortical, thalamic, and hippocampal cells of $(G_4C_2)_{66}$ animals (Fig. 2D-G, **Supplemental Fig. 2A-B**). The DPR positive cells within each brain region was quantified; the expression ranged from an average of approximately 30 cells per millimeter squared (mm^2) in the cortex for polyGA up to 150 cells

per mm^2 in the thalamus for polyGR. A significant increase in DPR positive cells in the $(G_4C_2)_{66}$ group was when compared to controls in all cases, except for polyGP positive cells in the cortex where there was significant variability between animals (Fig. 2C, 2E, 2G). In **Supplemental Fig. 1C**, we have illustrated the collective distribution of the DPR species that we observed in the brain of $(G_4C_2)_{66}$ animals.

In the spinal cord of $(G_4C_2)_{66}$ animals we found a less robust DPR burden than in the brain, in concordance with our polyGP MSD and RNAscope results (Fig. 2A; Fig. 1C). Specifically, we observed a significant increase in polyGP positive cells in the cervical spinal cord sections (gray matter and anterior horn), but on average we only observed between 3–5 positive cells per section (Fig. 2H-I). In lumbar spinal cord sections, we observed a slight but significant increase in polyGP positive cells in gray matter but not in the anterior horn (**Supplemental Fig. 2C**). There was no detectable expression of polyGR or polyGA positive cells in the spinal cord of $(G_4C_2)_{66}$ animals by IHC (data not shown).

TDP-43 and RanGTPase are functional in the C9ORF72 $(G_4C_2)_{66}$ mouse model

TDP-43 dysfunction is a hallmark feature in ALS, and several mouse models of ALS have recapitulated aggregated TDP-43 pathology *in situ* [45, 63]. We assessed the *C9ORF72* $(G_4C_2)_{66}$ mouse model for indicators of TDP-43 dysfunction. Loss of nuclear TDP-43 is an important event in ALS pathogenesis [65], thus we utilized immunostaining of total TDP-43 expression and localization as a readout for TDP-43 dysfunction. When we compared the expression of TDP-43 in neurons in the motor cortex of $(G_4C_2)_{66}$ animals to sham and $(G_4C_2)_2$ animals we did not observe any gross change in TDP-43 distribution or nuclear versus cytoplasmic (N/C) ratio (Fig. 3A-B). Moreover, we evaluated localization of TDP-43 in cells with significant DPR burden in various brain regions in $(G_4C_2)_{66}$ mice and did not observe mislocalization of TDP-43 in DPR positive cells (**Supplemental Fig. 3**). TDP-43 performs multiple functions, such as transcriptional repression, splicing, and translational regulation, that are disrupted in ALS [40, 76, 80]. The consequence of TDP-43 mislocalization can be evaluated by interrogating TDP-43 RNA targets [6, 33, 40, 46, 64]. We quantified the expression of several previously documented TDP-43 cryptic mRNA targets [86], that reflect loss of TDP-43 function, in the brain and spinal cord of $(G_4C_2)_{66}$ animals. When compared to control groups, we found that $(G_4C_2)_{66}$ animals had no significant change in the expression of *Grm2*, *Oasl1*, *Rspo1*, *Sort1*, *Tardbp*, *Tsn*, and *Unc13a* (Fig. 3C-D). Finally, we stained for RanGTPase as an indicator of nucleocytoplasmic transport (NCT) function in $(G_4C_2)_{66}$ animals, as loss of a steep nuclear-to-cytoplasmic RanGTPase gradient may lie upstream of TDP-43 dysfunction in ALS [13]. We observed a slight but significant increase in the RanGTPase N/C ratio in $(G_4C_2)_{66}$ compared to $(G_4C_2)_2$ animals, but not when $(G_4C_2)_{66}$ animals were compared to sham animals (Fig. 3E-F). Thus, it is unlikely that neither TDP-43 function or nucleocytoplasmic transport is significantly altered in the neurons of $(G_4C_2)_{66}$ mice.

Lack of Neuronal Degeneration but presence of P62-positive inclusions in the brain of C9ORF72 $(G_4C_2)_{66}$ mice

Disruptions in protein and RNA homeostasis as a result of an aberrant stress response have been implicated in the pathogenesis of C9 ALS [41]. To evaluate the *C9ORF72* $(G_4C_2)_{66}$ repeat expansion model for disturbances in protein homeostasis, we immunostained brain tissue for p62/Sqstm1, a protein that aggregates and associates with stress granules. We found p62-positive inclusions throughout the brain, including the cortex, hippocampus, and thalamus of 6-month old $(G_4C_2)_{66}$ animals (Fig. 4A). The number of p62-positive inclusions in all these brain regions was significantly increased in comparison to both sham and $(G_4C_2)_2$ animals (Fig. 4B). These data clearly indicate that the $(G_4C_2)_{66}$ repeat expansion leads to aberrant protein accumulation in the AAV-$(G_4C_2)_{66}$ mouse model.

The hallmark pathology of ALS is progressive degeneration of both upper and lower motor neurons. We assessed 6-month old mice injected with the $(G_4C_2)_{66}$ repeat expansion for neuronal loss by immunostaining brain and spinal cord sections with neuronal marker NeuN. The number of NeuN-positive neurons in the cortex of 7 sham, 5 $(G_4C_2)_2$ and 10 $(G_4C_2)_{66}$ animals was quantified (Fig. 4C-D). Surprisingly, we found that there was no significant difference in the number of NeuN-positive cells between groups. Next, we quantified the number of NeuN-positive cells in both cervical and lumbar spinal cord sections from control and $(G_4C_2)_{66}$ animals, where we also found that there was no difference between groups (Fig. 4E-F). Collectively, this lack of observed neuronal loss suggests that expression of the $(G_4C_2)_{66}$ construct does not cause apparent neurodegeneration in the $(G_4C_2)_{66}$ mouse model.

Mild gliosis is observed in the brain, but not the spinal cord of C9ORF72 $(G_4C_2)_{66}$ mice

We assessed the cellular response of astrocytes and microglia to the $(G_4C_2)_{66}$ repeat expansion with immunofluorescence and qRT-PCR at 6-month of age. First, we quantified glial fibrillary acidic protein (GFAP) immunoreactivity in brain and spinal cord sections. The percent GFAP-positive area did not significantly differ between sham, $(G_4C_2)_2$, and $(G_4C_2)_{66}$ animalswith sampling across the entire cortex or in cervical spinal cord tissue (Fig. 5A-B). Similarly, we quantified the GFAP-positive area in the motor cortex specifically and lumbar spinal cord and found no difference across experimental groups (**Supplemental Fig. 4A-B**). We utilized qRT-PCR for increased sensitivity to analyze *Gfap* expression in the brain and thoracic spinal cord tissue. Surprisingly, we found a significant increase in *Gfap* expression in the brain, but not the spinal cord of $(G_4C_2)_{66}$ animals in comparison to sham animals (Fig. 6A-B), suggesting there may be mild astrocyte reactivity in the brains of $(G_4C_2)_{66}$ animals.

To determine if microglia are responsive to the $(G_4C_2)_{66}$ repeat expansion, we quantified Iba1 immunoreactivity and morphology in the brain and spinal cord sections from all groups. There was no significant difference in the percent area that was Iba1-positive between 6-month old sham, $(G_4C_2)_2$, and $(G_4C_2)_{66}$ animals across brain and spinal cord sections (Fig. 5C-D, **Supplemental Fig. 4C-D**). Additionally,

there was no observable change to microglia morphology across all groups (data not shown). Next, we used qRT-PCR to assess the global expression of microglia markers, including *Aif1*, *Clec7a*, *Olfml3*, *Tmem119*, and *Trem2* (Fig. 6C-F). $(G_4C_2)_{66}$ animals had a significant increase in *Aif1* brain expression (Fig. 6C), suggesting there is a minor microglia response to the expression of the $(G_4C_2)_{66}$ repeat expression construct. Surprisingly, we also observed a slight but significant increase in Trem2 expression in (G4C2)2 animals but not (G4C2)66 animals in comparison to sham animals, which is likely due to inherent variability within the qPCR assay. However, we did not observe significant differences inany r glial activation indicators between $(G_4C_2)_2$ and $(G_4C_2)_{66}$ mice, so the minor glial activation profile in both (G4C2)2 and (G4C2)66 animals may be due to the injection procedure or the virus itself.

Lastly, we assessed the impact of $(G_4C_2)_{66}$ expression on systemic and CSF levels of neurofilament light chain (NfL) and GFAP. Despite no detectable loss of neurons and no apparent increase in GFAP immunoreactivity in CNS tissues, we found an increase in NfL concentration in both plasma and CSF compartments in 6-month old $(G_4C_2)_{66}$ animals compared to the sham group (Fig. 7A-B). The GFAP concentration measured in plasma from $(G_4C_2)_{66}$ animals was also increased compared to sham, but not in CSF (Fig. 7A-B).

C9ORF72 $(G_4C_2)_{66}$ mice do not have notable behavioral deficits

We evaluated the behavioral effects of the $(G_4C_2)_{66}$ repeat expansion with various behavioral tests including rotarod, grip strength, catwalk, and open-field assessment at 6-month of age. The study was powered based on rotarod as the primary end point, which indicated that the initial target sample size of n = 20 per group would provide 80% power to find significant differences as small as 23.3 seconds between groups on rotarod (see Randomization, Blinding, and Power section for details). There was no significant effect on bodyweight in $(G_4C_2)_{66}$ males from 90 dpi to 180 dpi compared to controls, while a slight decrease was notable in $(G_4C_2)_{66}$ females starting 146 dpi (**Supplemental Fig. 5A**). We assessed rotarod performance at 90 dpi and 180 dpi and found no significant difference between the experimental groups (Fig. 7C). After accounting for attrition among cohorts during the study, a post-hoc power analysis revealed that the final sample sizes (n = 32 Sham, n = 18 $(G_4C_2)_2$ and n = 35 $(G_4C_2)_{66}$) were sufficient to provide at least 80% power to detect a difference as small as 25 seconds in latency to fall on rotarod when comparing Sham or $(G_4C_2)_{66}$ to $(G_4C_2)_2$, and a difference as small as 20 seconds when comparing Sham to $(G_4C_2)_{66}$. Given that the observed differences among the groupsin this study were much smaller than 20 seconds, we can conclude that the lack of statistical significance among groups in the rotarod assay is not due to an insufficient sample size. We evaluated forelimb and hindlimb grip strength in females and males at 90 dpi and no significant difference was detected between groups (**Supplemental Fig. 5B**). Gait was assessed in the animals using Catwalk analysis, where no significant change to average speed, number of steps, or cadence was evident between the experimental groups (Fig. 7D). Finally, we used the open-field assay to evaluate general locomotor activity, exploration, and anxiety-like behavior in a novel environment at 180 dpi (Fig. 7E-F; **Supplemental Fig. 5C**). There was no

obvious or significant difference between the groups. Collectively, we did not observe any behavioral changes in the $(G_4C_2)_{66}$ animals unlike the previously reported study [10].

Discussion

ALS is a complex neurodegenerative disease that demonstrates regional specificity at onset and during progression along with highly consistent molecular pathologies [62]. Although sALS accounts for a significant portion (> 85%) of all cases, fALS has proven relatively more straightforward to study because of patient-derived induced pluripotent stem cells (which harbor the endogenous disease-causing mutations) and animal models that have been genetically modified to express disease-causing mutations in evolutionarily conserved genes [50, 63]. However, it is important to note that introduction of a mutation, or overexpression of human disease-associated proteins in non-human animals may not necessarily recapitulate all the physiological or pathological hallmarks of human disease. Here, we have evaluated histological, behavioral, and biochemical endpoints to determine which endophenotypes of human ALS/FTD are recapitulated in a previously published AAV2/9 *C9ORF72* $(G_4C_2)_{66}$ overexpression model [10] using a robust study design.

Firstly, this injection-based model leads to an extensive transduction of neurons throughout the brain and rostral segments of the spinal cord. We were able to detect the virally expressed repeat RNA in most brain regions and in cervical spinal cord but limited expression in lumbar spinal cord (refer to **Supplemental Fig. 1B**). We interrogated the expression of polyGP, one of the most abundant DPRs translated from repeat RNA, via MSD assay and immunohistochemistry. The polyGP MSD assay provided a sensitive but bulk assessment of brain and thoracic spinal cord samples, where polyGP burden was significantly elevated in the $(G_4C_2)_{66}$ animals. However, the burden of polyGP in thoracic spinal cord samples was approximately ten times less than that detected in the brain. Concordantly, there was notably lower poly-GP detected by immunohistochemistry in cervical spinal cord relative to the brain and even lower in the lumbar spinal cord, further corroborating a rostral-to-caudal decrease in viral expression and subsequent DPR expression. The other two DPRs, polyGA and polyGR, were detectable in the brain, but only minimally evident in the cervical spinal cord. Some polyGA and polyGR accumulations may be present in the lumbar spinal cord, though we were unable to faithfully detect the inclusions due to high background signal in control sections (data not shown). The decreasing trend in DPR abundance moving caudally throughout the spinal cord matches our observations that the repeat RNA is barely detectable in the lumbar spinal cord, though it is clearly visualized in the cervical region.

This observation, perhaps unsurprisingly, led us to question whether the $(G_4C_2)_{66}$ mice exhibit motor deficits, given the low abundance of repeat RNA and DPRs in the spinal cord. It has previously been reported that mice injected with the *C9ORF72* $(G_4C_2)_{66}$ viral construct fail to improve in daily rotarod tests relative to controls [10]. The authors did not observe motor deficits on the initial day of testing, yet a significant difference between $(G_4C_2)_{66}$ and control mice becomes evident after more than 2 days of consecutive rotarod tests. However, it is important to note that there was no baseline assessment prior

to these tests. In this study, we assessed latency to fall during a single day of rotarod testing at 90 dpi and 180 dpi with a well-powered sample size. There was no significant difference in the rotarod performance of $(G_4C_2)_{66}$ mice relative to sham or $(G_4C_2)_2$ controls. Moreover, we assessed various other metrics of motor function including grip strength and gait analysis and found no detectable difference in $(G_4C_2)_{66}$ mice compared to control groups. Given the lower burden of repeat RNA and DPRs in the spinal cord in mice we injected, we do not believe these mice demonstrate any primary deficits in motor function. Certainly others using the cerebral viral injection approach, as in the orginal study, may get different results, likely due to a differential delivery of the virus to the spinal cord. Alternatively it is possible that the high burden of repeat and DPRs in the motor cortex leads to a reduction in learned motor ability, which would become evident following multiple days of rotarod testing. Additionally, it would be intriguing to assess this model for memory deficits—as the significant DPR burden in the brain but limited expression in the spinal cord may have a greater impact on neurons involved in memory formation and retention.

Although there was no overt cellular loss observed in the CNS, there were hallmarks of cellular injury detected in the $(G_4C_2)_{66}$ animals. The increase in GFAP certainly reflects an astroglial response to cellular injury. Furthermore, the elevated NfL also is evidence for some neuronal injury as well. Differences between the current study and those of others may also reflect even small differences in viral uptake/delivery between labs. Nevertheless, the extent of this CNS injury was not sufficient to impair the various overall motor function or other behavioral measures, nor was it sufficient to be linked to any loss of TDP-43 function.

While loss of motor function is a consistent clinical characteristic of patients with ALS, there are many cellular and molecular signatures that allow clearer diagnosis postmortem. For example, nuclear clearance and loss of nuclear function of TDP-43, a nuclear DNA- and RNA-binding protein, is one of the most prominent pathological events preceding neuronal death [66, 70]. This pathology is present in the vast majority of ALS cases (> 97%) and is often co-observed with p62-positive granules [35]. We were unable to observe any significant nuclear clearance of TDP-43 in neurons of the motor cortex, despite the presence of p62-postive granules in this region. Since loss of TDP-43 nuclear function might occur prior to observed nuclear clearance by immunofluorescent assessment, we interrogated TDP-43 nuclear function by quantifying the abundance of multiple mRNA targets regulated by TDP-43. None of these targets, identified in previously published RNA-sequencing studies [86], demonstrated any significant alterations due to the presence of the *C9ORF72* $(G_4C_2)_{66}$ construct. This was true in both the thoracic spinal cord, where there is low viral burden, and the brain, which bears significant viral burden. Additionally, we observed no significant presence of phosphorylated TDP-43, a proposed pathogenic form, despite attempts with numerous commercial and custom pTDP-43 (Ser409/410) antibodies (data not shown) and no mislocalization of TDP-43 in cells positive for DPRs. Taken together, these findings provide evidence that, at least in the C57BL/6J mouse brain, overexpression of DPRs and repeat RNA in neurons does not lead to TDP-43 pathology or loss of function in 6-month-old (180 dpi) animals. Perhaps broader introduction of the virus to all cells within the central nervous system may lead to aberrant TDP-

43 pathology in neurons via non-cell autonomous effects, as this would more closely match the presence of the expanded repeat in human patients. Alternatively, this may be characteristic of interspecies differences.

There are more than ninety mouse models that have been generated to aid in the study of ALS [15]. Although there is significant redundancy when it comes to the genes being studied (for example, there are over thirty models to study TDP-43 alone), each model demonstrates unique strengths and weaknesses. While the *C9ORF72* $(G_4C_2)_{66}$ viral model we use in this study exhibits neither TDP-43 pathology nor primary motor deficits, the highly reliable and abundant RNA and DPR pathology makes it a useful tool to understand these pathological species' biogenesis, degradation, molecular associations, and traffic within and between cells. Use of this viral model would greatly complement studies that recapitulate more prominent aspects of ALS but fail to produce DPRs or repeat RNA at high enough levels to reliably investigate their pathology. Since ALS is such a heterogeneous disease in terms of genetic cause, onset, and progression, perhaps it is prudent to use multiple distinct models in each investigation. Though this will prove to be more costly and time consuming, it may lead to more reliable findings and results that ultimately represent human disease.

Conclusions

The viral vector delivery of the C9orf72 $(G_4C_2)_{66}$ mutant expansionof mice faithfully recapitulates the aberrant RNA and DPR pathology, typical of the human disease. Our findings indicate and support that this is a valuable, robust and pharmacologically tractable model for investigating the molecular mechanisms and cellular consequences of (G_4C_2) repeat driven DPR pathology. However, it does not exhibit a large signal for neuronal degradation or clinical disease. Important for studies of downstream ALS relevant cascades, this model does not show any evidence of impaired TAR DNA-binding protein-43 (TDP-43) function, as such it is not suitable for investigating the development of diseaseassociated with TDP-43 dysfunction. Our findings underscore the complexity of ALS pathogenesis involving genetic mutations and protein dysregulation and highlight the need for more comprehensive model systems that reliably replicate the multifaceted cellular and behavioral aspects of C9-ALS.

Abbreviations

AAV   Adeno associated virus

ALS   Amyotrophic lateral sclerosis

ANOVA   Analysis of variance

C9-ALS   Mutant C9orf72 ALS/FTD

DPR   Dipeptide repeat proteins

FTD   Frontotemporal dementia

GFAP   Glial fibrillary acidic protein

HRE   hexanucleotide repeat RNA expansion

MSD   Meso Scale discovery

N/C   Nuclear to cytoplasmic ration

NCT   Negative control

NfL   Neurofilament light chain

PBST   PBS with 0.05% Tween

polyGA   Poly Glycine-Alanine

polyGP   Glycine-Proline

polyGR   Glycine-Arginine

polyPA   Proline-Alanine

polyPR   Proline-Arginine

RAN   Repeat-associated non-ATG-dependent

sALS   Sporadic ALS

TDP-43   TAR DNA binding protein

Declarations

References

1. Alami NH, Smith RB, Carrasco MA, Williams LA, Winborn CS, Han SSW, Kiskinis E, Winborn B, Freibaum BD, Kanagaraj Aet al et al (2014) Axonal transport of TDP-43 mRNA granules is impaired by ALS-causing mutations. Neuron 81:536–543. 10.1016/j.neuron.2013.12.018

2. Arai T, Hasegawa M, Akiyama H, Ikeda K, Nonaka T, Mori H, Mann D, Tsuchiya K, Yoshida M, Hashizume Y al (2006) TDP-43 is a component of ubiquitin-positive tau-negative inclusions in frontotemporal lobar degeneration and amyotrophic lateral sclerosis. Biochem Biophys Res Commun 351:602–611. 10.1016/j.bbrc.2006.10.093

3. Ash PEA, Bieniek KF, Gendron TF, Caulfield T, Lin W-L, Dejesus-Hernandez M, van Blitterswijk MM, Jansen-West K, Paul JW 3rd, Rademakers R et al (2013) Unconventional translation of C9ORF72 GGGGCC expansion generates insoluble polypeptides specific to c9FTD/ALS. Neuron 77: 639–646 10.1016/j.neuron.2013.02.004

4. Barmada SJ, Skibinski G, Korb E, Rao EJ, Wu JY, Finkbeiner S (2010) Cytoplasmic mislocalization of TDP-43 is toxic to neurons and enhanced by a mutation associated with familial amyotrophic lateral sclerosis. J neuroscience: official J Soc Neurosci 30:639–649 Doi 10.1523/JNEUROSCI.4988 – 09.2010

5. Brettschneider J, Arai K, Del Tredici K, Toledo JB, Robinson JL, Lee EB, Kuwabara S, Shibuya K, Irwin DJ, Fang Let al et al (2014) TDP-43 pathology and neuronal loss in amyotrophic lateral sclerosis spinal cord. Acta Neuropathol 128:423–437. 10.1007/s00401-014-1299-6

6. Brown A-L, Wilkins OG, Keuss MJ, Hill SE, Zanovello M, Lee WC, Bampton A, Lee FCY, Masino L, Qi YA al (2022) TDP-43 loss and ALS-risk SNPs drive mis-splicing and depletion of UNC13A. Nature 603:131–137. 10.1038/s41586-022-04436-3

7. Buchman VL, Cooper-Knock J, Connor-Robson N, Higginbottom A, Kirby J, Razinskaya OD, Ninkina N, Shaw PJ (2013) Simultaneous and independent detection of C9ORF72 alleles with low and high number of GGGGCC repeats using an optimised protocol of Southern blot hybridisation. Mol Neurodegener 8:12–12. 10.1186/1750-1326-8-12

8. Carmen-Orozco RP, Tsao W, Ye Y, Sinha IR, Chang K, Trinh V, Chung W, Bowden K, Troncoso JC, Blackshaw Set al et al (2023) Elevated nuclear TDP-43 induces constitutive exon skipping. bioRxiv: Doi. 10.1101/2023.05.11.540291

9. Cheng W, Wang S, Zhang Z, Morgens DW, Hayes LR, Lee S, Portz B, Xie Y, Nguyen BV, Haney MS al (2019) CRISPR-Cas9 Screens Identify the RNA Helicase DDX3X as a Repressor of C9ORF72 (GGGGCC)n Repeat-Associated Non-AUG Translation. Neuron 104:885–898e888. 10.1016/j.neuron.2019.09.003

10. Chew J, Gendron TF, Prudencio M, Sasaguri H, Zhang Y-J, Castanedes-Casey M, Lee CW, Jansen-West K, Kurti A, Murray ME al (2015) Neurodegeneration. C9ORF72 repeat expansions in mice cause TDP-43 pathology, neuronal loss, and behavioral deficits. Sci (New York NY) 348:1151–1154. 10.1126/science.aaa9344

11. Chou C-C, Zhang Y, Umoh ME, Vaughan SW, Lorenzini I, Liu F, Sayegh M, Donlin-Asp PG, Chen YH, Duong DM et al (2018) TDP-43 pathology disrupts nuclear pore complexes and nucleocytoplasmic transport in ALS/FTD. Nat Neurosci 21: 228–239 10.1038/s41593-017-0047-3

12. Cooper-Knock J, Walsh MJ, Higginbottom A, Robin Highley J, Dickman MJ, Edbauer D, Ince PG, Wharton SB, Wilson SA, Kirby Jet al et al (2014) Sequestration of multiple RNA recognition motif-containing proteins by C9orf72 repeat expansions. Brain 137:2040–2051. 10.1093/brain/awu120

13. Coyne AN, Baskerville V, Zaepfel BL, Dickson DW, Rigo F, Bennett F, Lusk CP, Rothstein JD (2021) Nuclear accumulation of CHMP7 initiates nuclear pore complex injury and subsequent TDP-43 dysfunction in sporadic and familial ALS. Sci Transl Med 13: eabe1923. doi: 1910.1126/scitranslmed.abe1923 10.1126/scitranslmed.abe1923

14. Coyne AN, Zaepfel BL, Hayes L, Fitchman B, Salzberg Y, Luo EC, Bowen K, Trost H, Aigner S, Rigo Fet al et al (2020) G(4)C(2) Repeat RNA Initiates a POM121-Mediated Reduction in Specific Nucleoporins in C9orf72 ALS/FTD. Neuron 107: 1124–1140 e1111 10.1016/j.neuron.2020.06.027

15. De Giorgio F, Maduro C, Fisher EMC, Acevedo-Arozena A (2019) Transgenic and physiological mouse models give insights into different aspects of amyotrophic lateral sclerosis. Dis Model Mech 12:dmm037424. 037410.031242/dmm.037424

16. DeJesus-Hernandez M, Finch NA, Wang X, Gendron TF, Bieniek KF, Heckman MG, Vasilevich A, Murray ME, Rousseau L, Weesner R et al (2017) In-depth clinico-pathological examination of RNA foci in a large cohort of C9ORF72 expansion carriers. Acta Neuropathol 134: 255–269 10.1007/s00401-017-1725-7

17. DeJesus-Hernandez M, Mackenzie IR, Boeve BF, Boxer AL, Baker M, Rutherford NJ, Nicholson AM, Finch NA, Flynn H, Adamson Jet al et al (2011) Expanded GGGGCC hexanucleotide repeat in noncoding region of C9ORF72 causes chromosome 9p-linked FTD and ALS. Neuron 72:245–256. 10.1016/j.neuron.2011.09.011

18. Donnelly CJ, Zhang P-W, Pham JT, Haeusler AR, Mistry NA, Vidensky S, Daley EL, Poth EM, Hoover B, Fines DM al (2013) RNA toxicity from the ALS/FTD C9ORF72 expansion is mitigated by antisense intervention. Neuron 80:415–428. 10.1016/j.neuron.2013.10.015

19. Fallini C, Bassell GJ, Rossoll W (2012) The ALS disease protein TDP-43 is actively transported in motor neuron axons and regulates axon outgrowth. Hum Mol Genet 21:3703–3718. 10.1093/hmg/dds205

20. Freibaum BD, Lu Y, Lopez-Gonzalez R, Kim NC, Almeida S, Lee K-H, Badders N, Valentine M, Miller BL, Wong PC al (2015) GGGGCC repeat expansion in C9orf72 compromises nucleocytoplasmic transport. Nature 525:129–133. 10.1038/nature14974

21. Frick P, Sellier C, Mackenzie IRA, Cheng C-Y, Tahraoui-Bories J, Martinat C, Pasterkamp RJ, Prudlo J, Edbauer D, Oulad-Abdelghani M et al (2018) Novel antibodies reveal presynaptic localization of C9orf72 protein and reduced protein levels in C9orf72 mutation carriers. Acta neuropathologica communications 6: 72 – 70 10.1186/s40478-018-0579-0

22. Gal J, Strom A-L, Kwinter DM, Kilty R, Zhang J, Shi P, Fu W, Wooten MW, Zhu H (2009) Sequestosome 1/p62 links familial ALS mutant SOD1 to LC3 via an ubiquitin-independent mechanism. J Neurochem 111:1062–1073. 10.1111/j.1471-4159.2009.06388.x

23. Gendron TF, Bieniek KF, Zhang Y-J, Jansen-West K, Ash PEA, Caulfield T, Daughrity L, Dunmore JH, Castanedes-Casey M, Chew J al (2013) Antisense transcripts of the expanded C9ORF72 hexanucleotide repeat form nuclear RNA foci and undergo repeat-associated non-ATG translation in c9FTD/ALS. Acta Neuropathol 126:829–844. 10.1007/s00401-013-1192-8

24. Gendron TF, Chew J, Stankowski JN, Hayes LR, Zhang Y-J, Prudencio M, Carlomagno Y, Daughrity LM, Jansen-West K, Perkerson EA al (2017) Poly(GP) proteins are a useful pharmacodynamic marker for C9ORF72-associated amyotrophic lateral sclerosis. Sci Transl Med 9:eaai7866. 7810.1126/scitranslmed.aai7866

25. Gu J, Wu F, Xu W, Shi J, Hu W, Jin N, Qian W, Wang X, Iqbal K, Gong C-X al (2017) TDP-43 suppresses tau expression via promoting its mRNA instability. Nucleic Acids Res 45:6177–6193. 10.1093/nar/gkx175

26. Hao Z, Liu L, Tao Z, Wang R, Ren H, Sun H, Lin Z, Zhang Z, Mu C, Zhou J al (2019) Motor dysfunction and neurodegeneration in a C9orf72 mouse line expressing poly-PR. Nat Commun 10:2906–w. 10.1038/s41467-019-10956-w

27. Hartmann H, Hornburg D, Czuppa M, Bader J, Michaelsen M, Farny D, Arzberger T, Mann M, Meissner F, Edbauer D (2018) Proteomics and C9orf72 neuropathology identify ribosomes as poly-GR/PR interactors driving toxicity. Life science alliance 1: e201800070 10.26508/lsa.201800070

28. Igaz LM, Kwong LK, Lee EB, Chen-Plotkin A, Swanson E, Unger T, Malunda J, Xu Y, Winton MJ Trojanowski JQ (2011) Dysregulation of the ALS-associated gene TDP-43 leads to neuronal death and degeneration in mice. J Clin Investig 121: 726–738 10.1172/JCI44867

29. Iyer S, Subramanian V, Acharya KR (2018) C9orf72, a protein associated with amyotrophic lateral sclerosis (ALS) is a guanine nucleotide exchange factor. PeerJ 6:e5815. 10.7717/peerj.5815

30. Jiang J, Zhu Q, Gendron TF, Saberi S, McAlonis-Downes M, Seelman A, Stauffer JE, Jafar-Nejad P, Drenner K, Schulte D et al (2016) Gain of Toxicity from ALS/FTD-Linked Repeat Expansions in

C9ORF72 Is Alleviated by Antisense Oligonucleotides Targeting GGGGCC-Containing RNAs. Neuron 90: 535–550 10.1016/j.neuron.2016.04.006

31. Jones AR, Woollacott I, Shatunov A, Cooper-Knock J, Buchman V, Sproviero W, Smith B, Scott KM, Balendra R, Abel Oet al et al (2013) Residual association at C9orf72 suggests an alternative amyotrophic lateral sclerosis-causing hexanucleotide repeat. Neurobiol Aging 34:2234e2231–2234e2237. 10.1016/j.neurobiolaging.2013.03.003

32. Jovicic A, Mertens J, Boeynaems S, Bogaert E, Chai N, Yamada SB, Paul JW 3rd, Sun S, Herdy JR, Bieri Get al et al (2015) Modifiers of C9orf72 dipeptide repeat toxicity connect nucleocytoplasmic transport defects to FTD/ALS. Nat Neurosci 18:1226–1229. 10.1038/nn.4085

33. Kabashi E, Lin L, Tradewell ML, Dion PA, Bercier V, Bourgouin P, Rochefort D, Bel Hadj S, Durham HD, Vande Velde Cet al et al (2010) Gain and loss of function of ALS-related mutations of TARDBP (TDP-43) cause motor deficits in vivo. Hum Mol Genet 19:671–683. 10.1093/hmg/ddp534

34. Khalfallah Y, Kuta R, Grasmuck C, Prat A, Durham HD, Vande Velde C (2018) TDP-43 regulation of stress granule dynamics in neurodegenerative disease-relevant cell types. Sci Rep 8:7551–7550. 10.1038/s41598-018-25767-0

35. King A, Maekawa S, Bodi I, Troakes C, Al-Sarraj S (2011) Ubiquitinated, p62 immunopositive cerebellar cortical neuronal inclusions are evident across the spectrum of TDP-43 proteinopathies but are only rarely additionally immunopositive for phosphorylation-dependent TDP-43. Neuropathology: official J Japanese Soc Neuropathology 31:239–249. 10.1111/j.1440-1789.2010.01171.x

36. Klim JR, Williams LA, Limone F, Guerra San Juan I, Davis-Dusenbery BN, Mordes DA, Burberry A, Steinbaugh MJ, Gamage KK Kirchner R (2019) ALS-implicated protein TDP-43 sustains levels of STMN2, a mediator of motor neuron growth and repair. Nat Neurosci 22: 167–179 10.1038/s41593-018-0300-4

37. Kramer CY (1956) Extension of Multiple Range Tests to Group Means with Unequal Numbers of Replications. Biometrics 12. https://doi.org/10.2307/3001469

38. Kwon I, Xiang S, Kato M, Wu L, Theodoropoulos P, Wang T, Kim J, Yun J, Xie Y, McKnight SL (2014) Poly-dipeptides encoded by the C9orf72 repeats bind nucleoli, impede RNA biogenesis, and kill cells. Sci (New York NY) 345:1139–1145. 10.1126/science.1254917

39. Lee Y-B, Chen H-J, Peres JN, Gomez-Deza J, Attig J, Stalekar M, Troakes C, Nishimura AL, Scotter EL, Vance Cet al et al (2013) Hexanucleotide repeats in ALS/FTD form length-dependent RNA foci, sequester RNA binding proteins, and are neurotoxic. Cell Rep 5:1178–1186. 10.1016/j.celrep.2013.10.049

40. Ling JP, Pletnikova O, Troncoso JC, Wong PC (2015) TDP-43 repression of nonconserved cryptic exons is compromised in ALS-FTD. Sci (New York NY) 349:650–655. 10.1126/science.aab0983

41. Ling SC, Polymenidou M, Cleveland DW (2013) Converging mechanisms in als and FTD: Disrupted RNA and protein homeostasis. Neuron 79:416–438. 10.1016/j.neuron.2013.07.033

42. Liu Y, Pattamatta A, Zu T, Reid T, Bardhi O, Borchelt DR, Yachnis AT, Ranum LPW (2016) C9orf72 BAC Mouse Model with Motor Deficits and Neurodegenerative Features of ALS/FTD. Neuron 90:521–534. 10.1016/j.neuron.2016.04.005

43. Livak KJ, Schmittgen TD (2001) Analysis of relative gene expression data using real-time quantitative PCR and the 2(-Delta Delta C(T)) Method. Methods (San Diego Calif) 25:402–408. 10.1006/meth.2001.1262

44. Lopez-Gonzalez R, Lu Y, Gendron TF, Karydas A, Tran H, Yang D, Petrucelli L, Miller BL, Almeida S, Gao F-B (2016) Poly(GR) in C9ORF72-Related ALS/FTD Compromises Mitochondrial Function and Increases Oxidative Stress and DNA Damage in iPSC-Derived Motor Neurons. Neuron 92:383–391. 10.1016/j.neuron.2016.09.015

45. Lutz C (2018) Mouse models of ALS: Past, present and future. Brain Res 1693:1–10. 10.1016/j.brainres.2018.03.024

46. Ma XR, Prudencio M, Koike Y, Vatsavayai SC, Kim G, Harbinski F, Briner A, Rodriguez CM, Guo C, Akiyama Tet al et al (2022) TDP-43 represses cryptic exon inclusion in the FTD-ALS gene UNC13A. Nature 603:124–130. 10.1038/s41586-022-04424-7

47. Majounie E, Renton AE, Mok K, Dopper EGP, Waite A, Rollinson S, Chio A, Restagno G, Nicolaou N, Simon-Sanchez J et al (2012) Frequency of the C9orf72 hexanucleotide repeat expansion in patients with amyotrophic lateral sclerosis and frontotemporal dementia: a cross-sectional study. The LancetNeurology 11: 323–330 10.1016/S1474-4422(12)70043-1

48. McDonald KK, Aulas A, Destroismaisons L, Pickles S, Beleac E, Camu W, Rouleau GA, Vande Velde C (2011) TAR DNA-binding protein 43 (TDP-43) regulates stress granule dynamics via differential regulation of G3BP and TIA-1. Hum Mol Genet 20:1400–1410. 10.1093/hmg/ddr021

49. Mehta PR, Brown A-L, Ward ME, Fratta P (2023) The era of cryptic exons: implications for ALS-FTD. Mol Neurodegener 18: 16 – 15. 10.1186/s13024-023-00608-5

50. Mejzini R, Flynn LL, Pitout IL, Fletcher S, Wilton SD, Akkari PA (2019) ALS Genetics, Mechanisms, and Therapeutics: Where Are We. Now? Front Neurosci 13:1310. 10.3389/fnins.2019.01310

51. Mizielinska S, Gronke S, Niccoli T, Ridler CE, Clayton EL, Devoy A, Moens T, Norona FE, Woollacott IOC, Pietrzyk Jet al et al (2014) C9orf72 repeat expansions cause neurodegeneration in Drosophila through arginine-rich proteins. Sci (New York NY) 345:1192–1194. 10.1126/science.1256800

52. Mizielinska S, Lashley T, Norona FE, Clayton EL, Ridler CE, Fratta P, Isaacs AM (2013) C9orf72 frontotemporal lobar degeneration is characterised by frequent neuronal sense and antisense RNA foci. Acta Neuropathol 126:845–857. 10.1007/s00401-013-1200-z

53. Mizuno Y, Amari M, Takatama M, Aizawa H, Mihara B, Okamoto K (2006) Immunoreactivities of p62, an ubiqutin-binding protein, in the spinal anterior horn cells of patients with amyotrophic lateral sclerosis. J Neurol Sci 249:13–18. 10.1016/j.jns.2006.05.060

54. Moazami MP, Rembetsy-Brown JM, Wang F, Krishnamurthy PM, Weiss A, Marosfoi M, King RM, Motwani M, Gray-Edwards H, Fitzgerald KA al (2021) Quantifying and Mitigating Motor Phenotypes

Induced by Antisense Oligonucleotides in the Central Nervous System. bioRxiv: 2021.2002.2014.431096. 10.1101/2021.02.14.431096

55. Mordes DA, Morrison BM, Ament XH, Cantrell C, Mok J, Eggan P, Xue C, Wang J-Y, Eggan K, Rothstein JD (2020) Absence of Survival and Motor Deficits in 500 Repeat C9ORF72 BAC Mice. Neuron 108:775–783e774. 10.1016/j.neuron.2020.08.009

56. Mori K, Arzberger T, Grasser FA, Gijselinck I, May S, Rentzsch K, Weng S-M, Schludi MH, van der Zee J, Cruts M et al (2013) Bidirectional transcripts of the expanded C9orf72 hexanucleotide repeat are translated into aggregating dipeptide repeat proteins. Acta Neuropathol 126: 881–893 10.1007/s00401-013-1189-3

57. Mori K, Weng S-M, Arzberger T, May S, Rentzsch K, Kremmer E, Schmid B, Kretzschmar HA, Van Cruts M, Broeckhoven Cet al et al (2013) The C9orf72 GGGGCC repeat is translated into aggregating dipeptide-repeat proteins in FTLD/ALS. Science (New York, NY) 339: 1335–1338 10.1126/science.1232927

58. Neumann M, Sampathu D, Kwong L, Truax A, Micsenyi M, Chou T, Bruce J, Schuch T, Grossman M, Clark Cet al et al (2006) Ubiquitinated TDP-43 in Frontotemporal Lobar Degeneration and Amyotorphic Lateral Sclerosis. Science 314:130–133. 10.1002/ana.21425.Phosphorylated

59. Nguyen L, Laboissonniere LA, Guo S, Pilotto F, Scheidegger O, Oestmann A, Hammond JW, Li H, Hyysalo A, Peltola R al (2020) Survival and Motor Phenotypes in FVB C9-500 ALS/FTD BAC Transgenic Mice Reproduced by Multiple Labs. Neuron 108:784–796e783. 10.1016/j.neuron.2020.09.009

60. O'Rourke JG, Bogdanik L, Muhammad AKMG, Gendron TF, Kim KJ, Austin A, Cady J, Liu EY, Zarrow J, Grant Set al et al (2015) C9orf72 BAC Transgenic Mice Display Typical Pathologic Features of ALS/FTD. Neuron 88:892–901. 10.1016/j.neuron.2015.10.027

61. Peters OM, Cabrera GT, Tran H, Gendron TF, McKeon JE, Metterville J, Weiss A, Wightman N, Salameh J, Kim J al (2015) Human C9ORF72 Hexanucleotide Expansion Reproduces RNA Foci and Dipeptide Repeat Proteins but Not Neurodegeneration in BAC Transgenic Mice. Neuron 88:902–909. 10.1016/j.neuron.2015.11.018

62. Peters OM, Ghasemi M, Brown RH Jr (2015) Emerging mechanisms of molecular pathology in ALS. J Clin Investig 125:1767–1779. 10.1172/JCI71601

63. Philips T, Rothstein JD (2015) Rodent Models of Amyotrophic Lateral Sclerosis. Curr Protoc Pharmacol 69: 5.67.61–65.67.21 10.1002/0471141755.ph0567s69

64. Polymenidou M, Cleveland DW (2011) The seeds of neurodegeneration: prion-like spreading in ALS. Cell 147:498–508. 10.1016/j.cell.2011.10.011

65. Prasad A, Bharathi V, Sivalingam V, Girdhar A, Patel BK (2019) Molecular Mechanisms of TDP-43 Misfolding and Pathology in Amyotrophic Lateral Sclerosis. Front Mol Neurosci 12:25. 10.3389/fnmol.2019.00025

66. Reale LA, Dyer MS, Perry SE, Young KM, Dickson TC, Woodhouse A, Blizzard CA (2023) Pathologically mislocalised TDP-43 in upper motor neurons causes a die-forward spread of ALS-like

pathogenic changes throughout the mouse corticomotor system. Prog Neurobiol 226:102449. 10.1016/j.pneurobio.2023.102449

67. Renton AE, Majounie E, Waite A, Simon-Sanchez J, Rollinson S, Gibbs JR, Schymick JC, Laaksovirta H, van Swieten JC, Myllykangas Let al et al (2011) A hexanucleotide repeat expansion in C9ORF72 is the cause of chromosome 9p21-linked ALS-FTD. Neuron 72:257–268. 10.1016/j.neuron.2011.09.010

68. Richner M, Jager SB, Siupka P, Vaegter CB (2017) Hydraulic Extrusion of the Spinal Cord and Isolation of Dorsal Root Ganglia in Rodents. J visualized experiments: JoVE 11955226. 10.3791/55226

69. Riemslagh FW, van der Toorn EC, Verhagen RFM, Maas A, Bosman LWJ, Hukema RK, Willemsen R (2021) Inducible expression of human C9ORF72 36x G(4)C(2) hexanucleotide repeats is sufficient to cause RAN translation and rapid muscular atrophy in mice. Dis Model Mech 14:dmm044842. 044810.041242/dmm.044842

70. Scotter EL, Chen H-J, Shaw CE (2015) TDP-43 Proteinopathy and ALS: Insights into Disease Mechanisms and Therapeutic Targets. Neurotherapeutics: J Am Soc Experimental Neurother 12:352–363. 10.1007/s13311-015-0338-x

71. Simon-Sanchez J, Dopper EGP, Cohn-Hokke PE, Hukema RK, Nicolaou N, Seelaar H, de Graaf JRA, de Koning I, van Schoor NM, Deeg DJHet al et al (2012) The clinical and pathological phenotype of C9ORF72 hexanucleotide repeat expansions. Brain 135:723–735. 10.1093/brain/awr353

72. Sleigh JN, Tosolini AP, Gordon D, Devoy A, Fratta P, Fisher EMC, Talbot K, Schiavo G (2020) Mice Carrying ALS Mutant TDP-43, but Not Mutant FUS, Display In Vivo Defects in Axonal Transport of Signaling Endosomes. Cell Rep 30:3655–3662e3652. 10.1016/j.celrep.2020.02.078

73. Spead O, Zaepfel BL, Rothstein JD (2022) Nuclear Pore Dysfunction in Neurodegeneration. Neurotherapeutics: J Am Soc Experimental Neurother 19:1050–1060. 10.1007/s13311-022-01293-w

74. Stewart H, Rutherford NJ, Briemberg H, Krieger C, Cashman N, Fabros M, Baker M, Fok A, DeJesus-Hernandez M, Eisen A al (2012) Clinical and pathological features of amyotrophic lateral sclerosis caused by mutation in the C9ORF72 gene on chromosome 9p. Acta Neuropathol 123:409–417. 10.1007/s00401-011-0937-5

75. Su Z, Zhang Y, Gendron TF, Bauer PO, Chew J, Yang W-Y, Fostvedt E, Jansen-West K, Belzil VV, Desaro Pet al et al (2014) Discovery of a biomarker and lead small molecules to target r(GGGGCC)-associated defects in c9FTD/ALS. Neuron 83:1043–1050. 10.1016/j.neuron.2014.07.041

76. Suk TR, Rousseaux MWC (2020) The role of TDP-43 mislocalization in amyotrophic lateral sclerosis. Mol Neurodegener 15: 45 – 41. 10.1186/s13024-020-00397-1

77. Tanji K, Zhang H-X, Mori F, Kakita A, Takahashi H, Wakabayashi K (2012) p62/sequestosome 1 binds to TDP-43 in brains with frontotemporal lobar degeneration with TDP-43 inclusions. J Neurosci Res 90:2034–2042. 10.1002/jnr.23081

78. Tong J, Huang C, Bi F, Wu Q, Huang B, Liu X, Li F, Zhou H, Xia X-G (2013) Expression of ALS-linked TDP-43 mutant in astrocytes causes non-cell-autonomous motor neuron death in rats. EMBO J 32:1917–1926. 10.1038/emboj.2013.122

79. Tukey JW (1949) Comparing individual means in the analysis of variance. Biometrics 5:99–114

80. Van Deerlin VM, Leverenz JB, Bekris LM, Bird TD, Yuan W, Elman LB, Clay D, Wood EM, Chen-Plotkin AS Martinez-Lage M (2008) TARDBP mutations in amyotrophic lateral sclerosis with TDP-43 neuropathology: a genetic and histopathological analysis. Lancet Neurol 7: 409–416 10.1016/S1474-4422(08)70071-1

81. Van Langenhove T, van der Zee J, Van Broeckhoven C (2012) The molecular basis of the frontotemporal lobar degeneration-amyotrophic lateral sclerosis spectrum. Ann Med 44:817–828. 10.3109/07853890.2012.665471

82. Vatsavayai SC, Nana AL, Yokoyama JS, Seeley WW (2019) C9orf72-FTD/ALS pathogenesis: evidence from human neuropathological studies. Acta Neuropathol 137:1–26. 10.1007/s00401-018-1921-0

83. Verdone BM, Cicardi ME, Wen X, Sriramoji S, Russell K, Markandaiah SS, Jensen BK, Krishnamurthy K, Haeusler AR, Pasinelli Pet al et al (2022) A mouse model with widespread expression of the C9orf72-linked glycine-arginine dipeptide displays non-lethal ALS/FTD-like phenotypes. Sci Rep 12:5644–z. 10.1038/s41598-022-09593-z

84. Waite AJ, Baumer D, East S, Neal J, Morris HR, Ansorge O, Blake DJ (2014) Reduced C9orf72 protein levels in frontal cortex of amyotrophic lateral sclerosis and frontotemporal degeneration brain with the C9ORF72 hexanucleotide repeat expansion. Neurobiol Aging 35:1779e1775–1779e1713. 10.1016/j.neurobiolaging.2014.01.016

85. Wen X, Tan W, Westergard T, Krishnamurthy K, Markandaiah SS, Shi Y, Lin S, Shneider NA, Monaghan J, Pandey, UBet al (2014) Antisense proline-arginine RAN dipeptides linked to C9ORF72-ALS/FTD form toxic nuclear aggregates that initiate in vitro and in vivo neuronal death. Neuron 84:1213–1225. 10.1016/j.neuron.2014.12.010

86. Wu L-S, Cheng W-C, Chen C-Y, Wu M-C, Wang Y-C, Tseng Y-H, Chuang T-J, Shen CKJ (2019) Transcriptomopathies of pre- and post-symptomatic frontotemporal dementia-like mice with TDP-43 depletion in forebrain neurons. Acta Neuropathol Commun 7:50–x. 10.1186/s40478-019-0674-x

87. Xu Y-F, Prudencio M, Hubbard JM, Tong J, Whitelaw EC, Jansen-West K, Stetler C, Cao X, Song J, Zhang Y-J (2013) The pathological phenotypes of human TDP-43 transgenic mouse models are independent of downregulation of mouse Tdp-43. PLoS ONE 8:e69864. 10.1371/journal.pone.0069864

88. Zhang K, Daigle JG, Cunningham KM, Coyne AN, Ruan K, Grima JC, Bowen KE, Wadhwa H, Yang P, Rigo F et al (2018) Stress Granule Assembly Disrupts Nucleocytoplasmic Transport. Cell 173: 958–971 e917 10.1016/j.cell.2018.03.025

89. Zhang Y-J, Gendron TF, Grima JC, Sasaguri H, Jansen-West K, Xu Y-F, Katzman RB, Gass J, Murray ME, Shinohara Met al et al (2016) C9ORF72 poly(GA) aggregates sequester and impair HR23 and nucleocytoplasmic transport proteins. Nat Neurosci 19:668–677. 10.1038/nn.4272

90. Zhang Y-J, Jansen-West K, Xu Y-F, Gendron TF, Bieniek KF, Lin W-L, Sasaguri H, Caulfield T, Hubbard J, Daughrity L et al et al (2014) Aggregation-prone c9FTD/ALS poly(GA) RAN-translated proteins cause neurotoxicity by inducing ER stress. Acta Neuropathol 128:505–524. 10.1007/s00401-014-1336-5
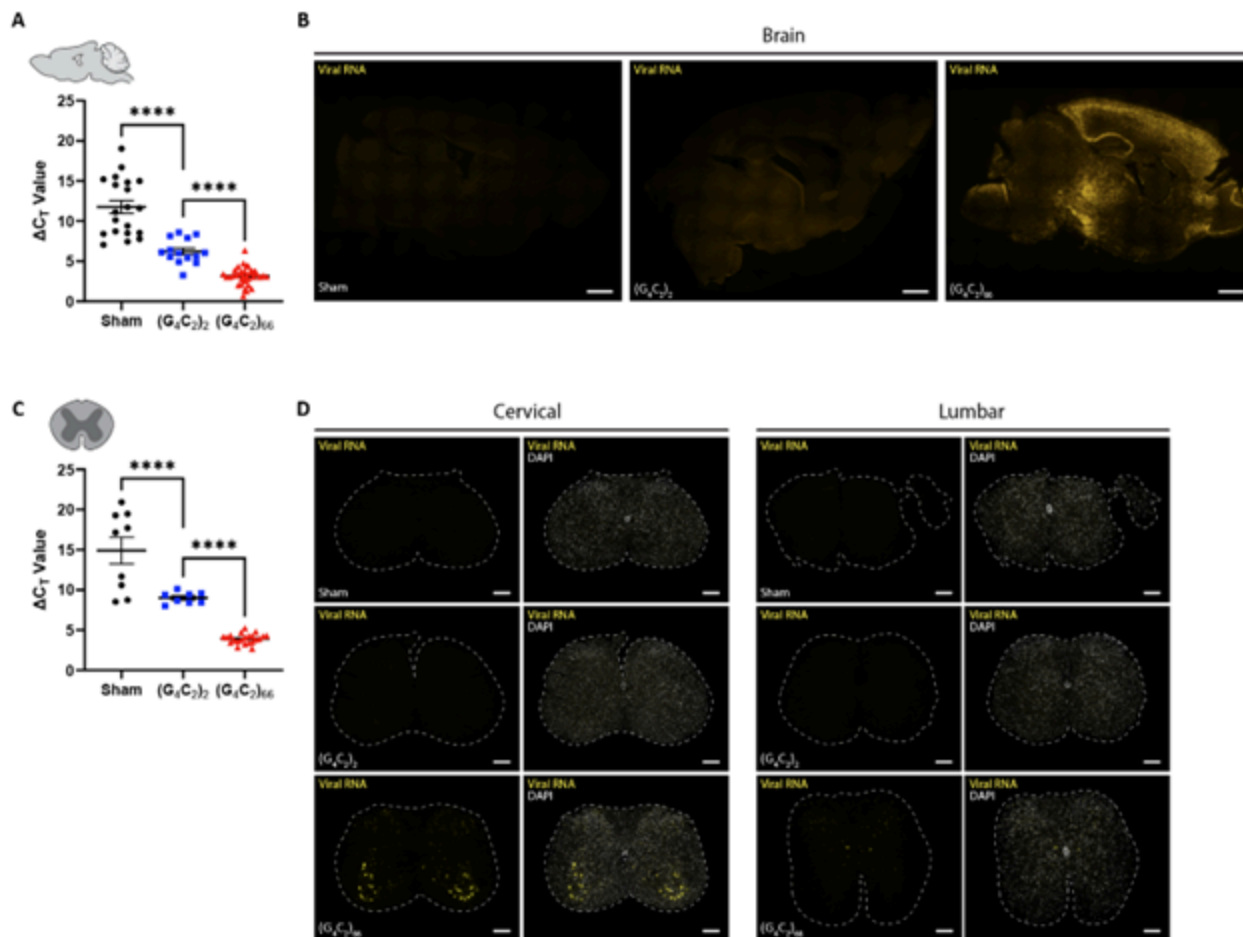
Figures

Figure 1

The $(G_4C_2)_{66}$ viral construct is expressed in brain and spinal cord following intraventricular delivery.
Isolated RNA samples from brain (sham n=20, $(G_4C_2)_2$ n=14, $(G_4C_2)_{66}$ n=34) **(A)** and thoracic spinal cord (sham n=9, $(G_4C_2)_2$ n=8, $(G_4C_2)_{66}$ n=22), error bars = SEM **(C)** were analyzed by qRT-PCR for the expression of the WPRE region of the viral construct. Outliers were identified with the ROUT test (Q=1%) and removed from the dataset. One-way ANOVA analysis of brain (p <0.0001) and spinal cord (p<0.0001) was performed, followed by Tukey's multiple comparisons test (brain: sham vs. $(G_4C_2)_2$ p<0.0001, $(G_4C_2)_2$ vs. $(G_4C_2)_{66}$ p<0.0001; spinal cord: sham vs. $(G_4C_2)_2$ p<0.0001, $(G_4C_2)_2$ vs. $(G_4C_2)_{66}$ p<0.0001) , error bars = SEM. Formalin-fixed paraffin-embedded sections from brain and spinal cord sections were analyzed for WPRE expression by RNAScope. Representative images in brain and spinal cord are shown

in **(B)** and **(D)**, respectively (sham n=3, $(G_4C_2)_2$ n=3, $(G_4C_2)_{66}$ n=6). Scale bars 1000 μm in (B) and 200 μm in (D).
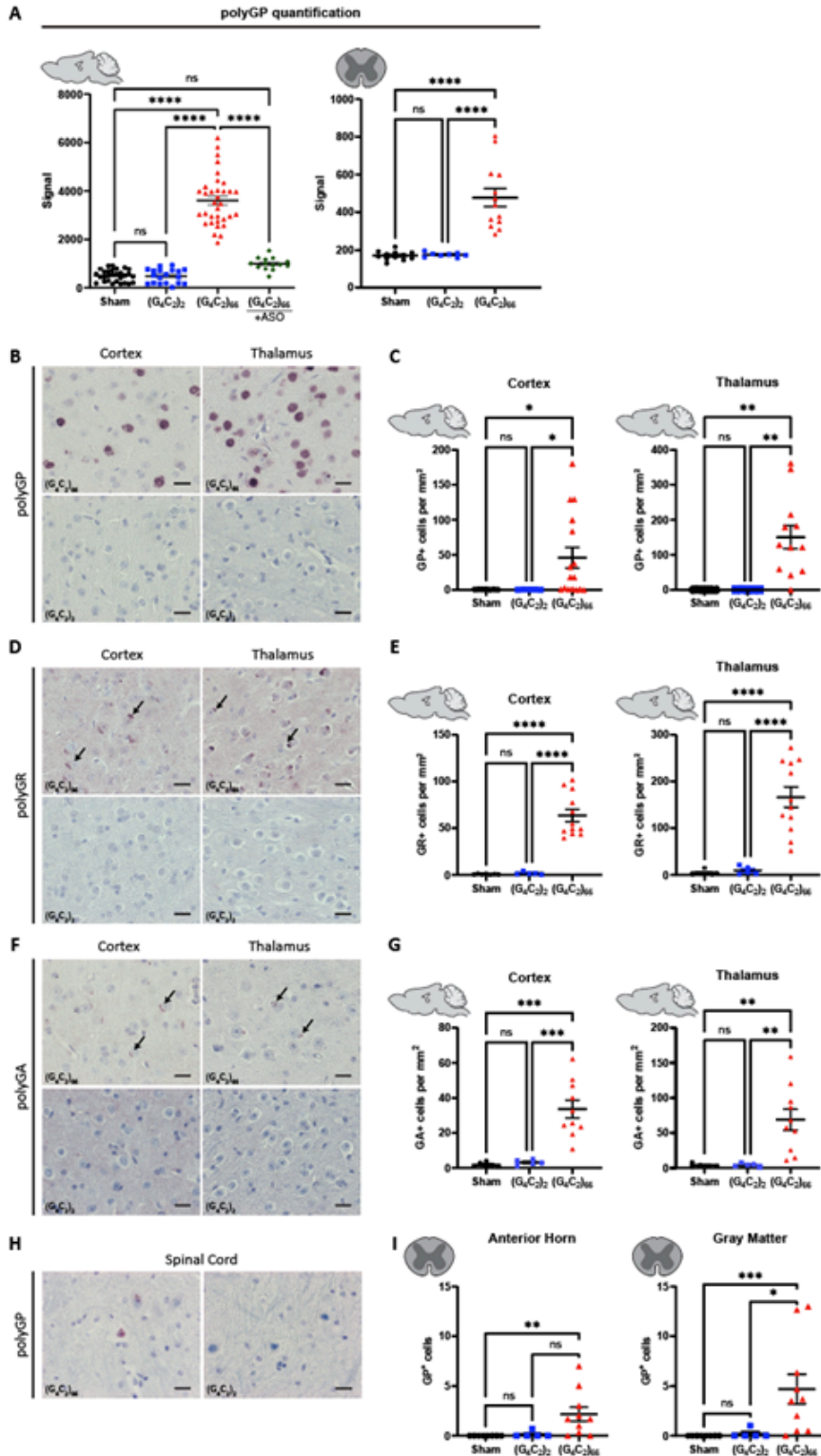

Figure 2

$(G_4C_2)_{66}$ mice have DPR expression in the brain and spinal cord. **(A)** Brain (sham n=29, $(G_4C_2)_2$ n=19, $(G_4C_2)_{66}$ n=34, $(G_4C_2)_{66}$ +C9-ASO n=14) and thoracic spinal cord (sham n=12, $(G_4C_2)_2$ n=8, $(G_4C_2)_{66}$ n=13) tissue lysates were analyzed by Meso Scale Discovery assay for the expression of polyGP dipeptide

repeat. One-way ANOVA analysis of brain (p <0.0001) and spinal cord (p<0.0001) was performed, followed by Tukey's multiple comparisons test (brain: sham vs. $(G_4C_2)_2$ p=0.9996, sham vs. $(G_4C_2)_{66}$ p<0.0001, $(G_4C_2)_2$ vs. $(G_4C_2)_{66}$ p<0.0001, sham vs. $(G_4C_2)_{66}$ +C9-ASO p=0.1123, $(G_4C_2)_{66}$ vs. $(G_4C_2)_{66}$ + C9-ASO p<0.0001; spinal cord: sham vs. $(G_4C_2)_2$ p=0.9958, sham vs. $(G_4C_2)_{66}$ p<0.0001, $(G_4C_2)_2$ vs. $(G_4C_2)_{66}$ p<0.001, error bars = SEM. **(B)** Representative images of brain sections stained for polyGP. Scale bars 20 µm. **(C)** Quantification of polyGP positive cells in cortex and thalamus region (sham n=7, $(G_4C_2)_2$ n=5, $(G_4C_2)_{66}$ n=16 for cortex, 12 for hippocampus and thalamus). One-way Welch ANOVA analysis (Welch, 1947) of polyGP positive cell number was performed (p=0.0021 for cortex and p=0.0002 for thalamus) followed by Tukey's multiple comparison test. Cortex: sham vs $(G_4C_2)_2$ p=0.4842, sham vs $(G_4C_2)_{66}$ p=0.0220 and $(G_4C_2)_2$ vs $(G_4C_2)_{66}$ p=0.0215, Thalamus: sham vs $(G_4C_2)_2$ p>0.9999, sham vs $(G_4C_2)_{66}$ p=0.0023 and $(G_4C_2)_2$ vs $(G_4C_2)_{66}$ p=0.0023, error bars = SEM. **(D)** Representative images of brain sections stained for polyGR. Scale bars 20 µm. **(E)** Quantification of polyGR positive cells in cortex and thalamus region (sham n=7, $(G_4C_2)_2$ n=5, $(G_4C_2)_{66}$ n=12). One-way Welch ANOVA analysis of polyGR positive cell number was performed (p<0.0001 for cortex and thalamus) followed by Tukey's multiple comparison test. Cortex: sham vs $(G_4C_2)_2$ p=0.4769, sham vs $(G_4C_2)_{66}$ p<0.0001 and $(G_4C_2)_2$ vs $(G_4C_2)_{66}$ p<0.0001, Thalamus: sham vs $(G_4C_2)_2$ p=0.5929, sham vs $(G_4C_2)_{66}$ p<0.0001 and $(G_4C_2)_2$ vs $(G_4C_2)_{66}$ p<0.0001, error bars = SEM. **(F)** Representative images of brain sections stained for polyGA. Scale bars 20µm. **(G)** Quantification of polyGA positive cells in cortex and thalamus region (sham n=6 for cortex, 5 for thalamus and hippocampus, $(G_4C_2)_2$ n=5, $(G_4C_2)_{66}$ n=10 for cortex and thalamus, 9 for hippocampus). One-way Welch ANOVA analysis of polyGA positive cell number was performed (p<0.0001 for cortex and p=0.0006 for thalamus) followed by Tukey's multiple comparison test. Cortex: sham vs $(G_4C_2)_2$ p=0.3688, sham vs $(G_4C_2)_{66}$ p=0.0004 and $(G_4C_2)_2$ vs $(G_4C_2)_{66}$ p=0.0006, Thalamus: sham vs $(G_4C_2)_2$ p=0.9980, sham vs $(G_4C_2)_{66}$ p=0.0056 and $(G_4C_2)_2$ vs $(G_4C_2)_{66}$ p=0.0057, error bars = SEM. **(H)** Representative images of cervical spinal cord sections stained against polyGP. Scale bars 20 µm. **(I)** Quantification of cervical spinal cord sections stained against polyGP (sham n=8, $(G_4C_2)_2$ n=5, $(G_4C_2)_{66}$ n=10). A Kruskal-Wallis test (Kruskal, Wallis 1952) on the cervical spinal cord gray matter (p=0.0006) and anterior horn (p=0.0018) was performed, followed by Dunn's multiple comparisons test (Dunn, 1964) (gray matter: sham vs. $(G_4C_2)_2$ p>0.9999, sham vs. $(G_4C_2)_{66}$ p=0.0008, $(G_4C_2)_2$ vs. $(G_4C_2)_{66}$ p=0.0266; anterior horn: sham vs. $(G_4C_2)_2$ p>0.9999, sham vs. $(G_4C_2)_{66}$ p=0.0024, $(G_4C_2)_2$ vs. $(G_4C_2)_{66}$ p=0.0512), error bars = SEM.

Figure 3
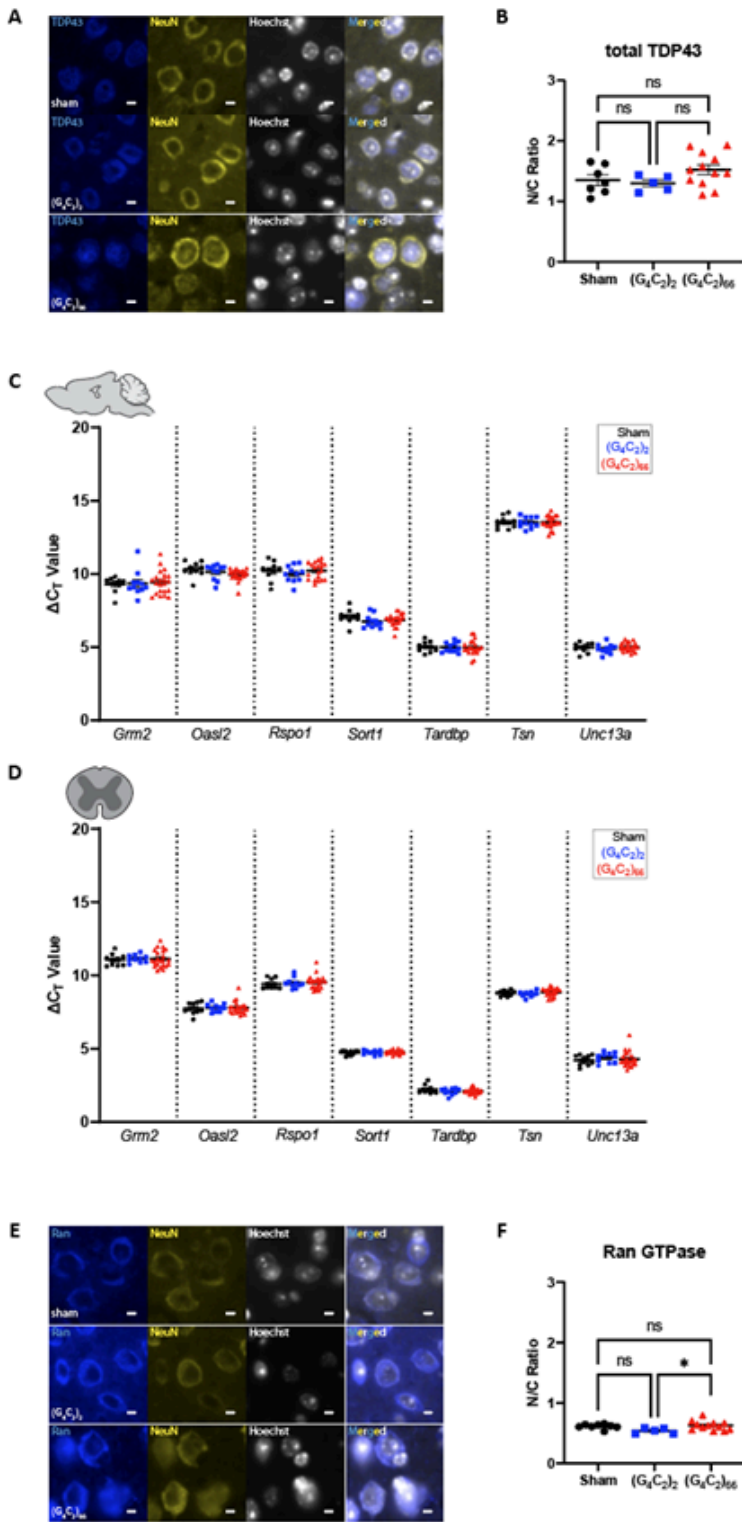
No evidence for loss of TDP-43 or RanGTPase function in the $(G_4C_2)_{66}$ mouse model. **(A)** Representative images of immunohistochemistry analysis of TDP-43 expression within the motor cortex tissue. Scale bars 5 μm. **(B)** Quantification of nuclear to cytoplasmic ratio of TDP-43 (sham n=7, $(G_4C_2)_2$ n=5, $(G_4C_2)_{66}$ n=12). One-way ANOVA: p=0.1597, Tukey's multiple comparisons test: sham vs. $(G_4C_2)_2$ p=0.9297, sham

vs. $(G_4C_2)_{66}$ p=0.3097, $(G_4C_2)_2$ vs. $(G_4C_2)_{66}$ p=0.2129. The expression of several TDP-43 mRNA targets was analyzed by qRT-PCR in samples from **(C)** brain (sham n=10, $(G_4C_2)_2$ n=11, $(G_4C_2)_{66}$ n=21) and **(D)** thoracic spinal cord (sham n=10, $(G_4C_2)_2$ n=10, $(G_4C_2)_{66}$ n=22) tissue. Outliers were identified with the ROUT test (Q=1%) and removed from the dataset. A one-way ANOVA was performed for each gene independently and no significant statistical difference was found in brain (*Grm2*: p=0.8822; *Oasl2*: p=0.1082; *Rspo1*: p=0.5920; *Sort1*: p=0.5175; *Tardbp*: p=0.9677; *Tsn*: p=0.9973; *Unc13a*: p=0.5271) or spinal cord (*Grm2*: p=0.9061; *Oasl2*: p=0.9364; *Rspo1*: p=0.7679; *Sort1*: p=0.6396; *Tardbp*: p=0.2842; *Tsn*: p=0.3036; *Unc13a*: p=0.6663) , error bars = SEM. **(E)** Representative images of immunohistochemistry analysis of RanGTPase analysis within the motor cortex tissue. Scale bars 5 µm. **(F)** Quantification of nuclear to cytoplasmic ratio of RanGTPase (sham n=8, $(G_4C_2)_2$ n=5, $(G_4C_2)_{66}$ n=12). One-way ANOVA: p=0.0401, Tukey's multiple comparisons test: sham vs. $(G_4C_2)_2$ p=0.1101, sham vs. $(G_4C_2)_{66}$ p=0.8696, $(G_4C_2)_2$ vs. $(G_4C_2)_{66}$ p=0.0339, error bars = SEM.
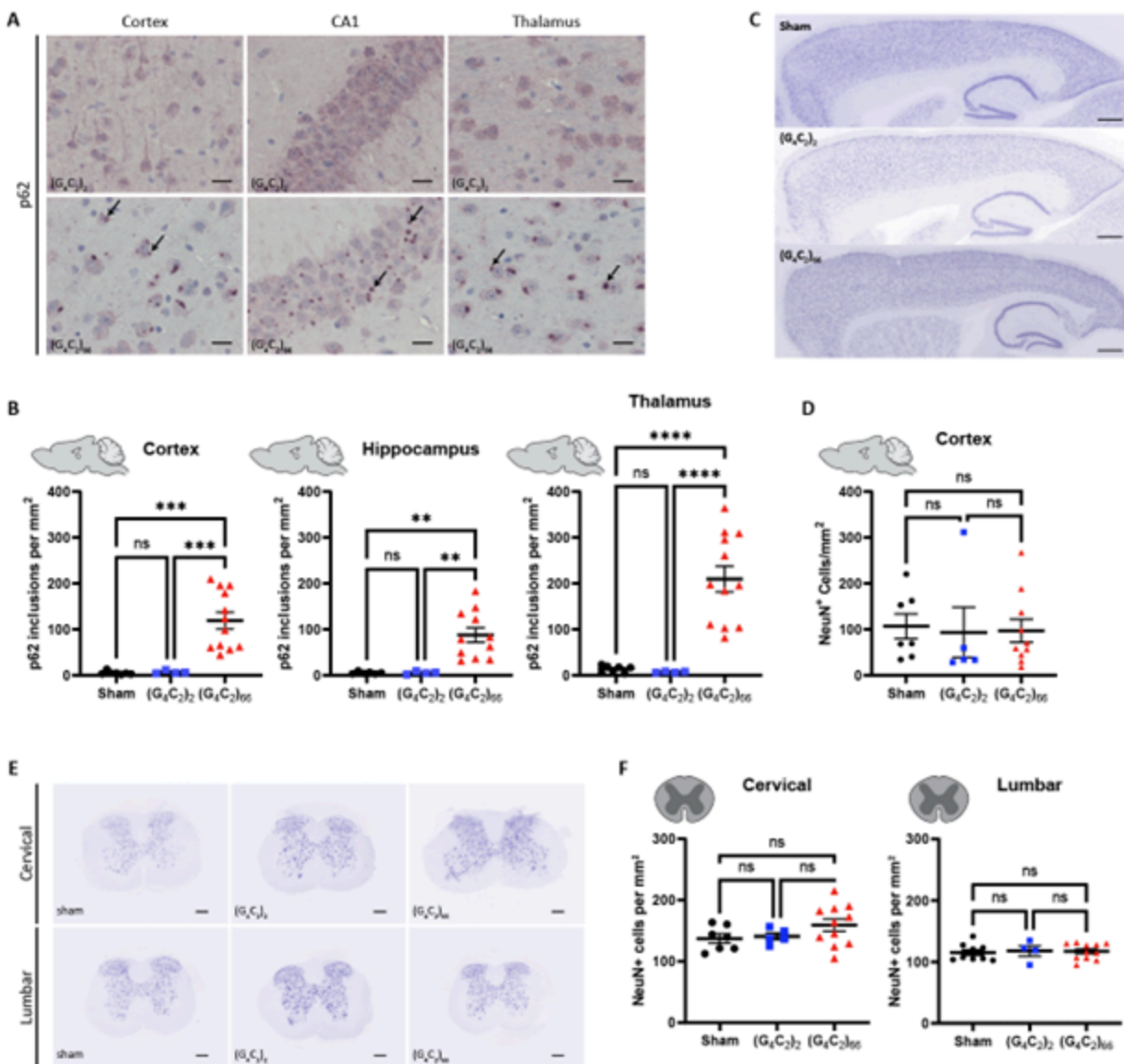

Figure 4

Analysis of p62 inclusions and neuronal count in the $(G_4C_2)_{66}$ mouse model. **(A)** Representative images of brain sections stained against p62. As pointed by the arrows, p62 positive inclusions are mostly seen in 6-month old $(G_4C_2)_{66}$ mice and not in sham or $(G_4C_2)_2$ mice. Scale bars 20 μm. **(B)** Quantification of p62 inclusions in cortex, thalamus, and hippocampus region (sham n=7 for thalamus and cortex, $(G_4C_2)_2$ n=4, $(G_4C_2)_{66}$ n=12 for cortex and thalamus, 11 for hippocampus). One-way Welch ANOVA analysis of p62 inclusions was performed (p<0.0001 for cortex, thalamus, and hippocampus) followed by Tukey's multiple comparison test. Cortex: sham vs $(G_4C_2)_2$ p=0.7421, sham vs $(G_4C_2)_{66}$ p=0.0002 and $(G_4C_2)_2$ vs $(G_4C_2)_{66}$ p=0.0002, Thalamus: sham vs $(G_4C_2)_2$ p=0.1518, sham vs $(G_4C_2)_{66}$ p<0.0001 and $(G_4C_2)_2$ vs $(G_4C_2)_{66}$ p<0.0001, Hippocampus: sham vs $(G_4C_2)_2$ p=0.9997, sham vs $(G_4C_2)_{66}$ p=0.0011 and $(G_4C_2)_2$ vs $(G_4C_2)_{66}$ p=0.0011, error bars = SEM. **(C)** Representative images of brain sections from 6-month old animals stained against NeuN. **(D)** Quantification of NeuN positive cells within the cortex (sham n=7, $(G_4C_2)_2$ n=5, $(G_4C_2)_{66}$ n=10). Scale bars 500 μm. One-way ANOVA: p=0.9601, Tukey's multiple comparisons test: sham vs. $(G_4C_2)_2$ p=0.9631, sham vs. $(G_4C_2)_{66}$ p=0.9714, $(G_4C_2)_2$ vs. $(G_4C_2)_{66}$ p=0.9971, error bars = SEM. **(E)** Representative cervical and lumbar spinal cord sections stained against NeuN. Scale bars 200 μm. **(F)** Quantification of NeuN positive cells within the cervical (sham n=7, $(G_4C_2)_2$ n=5, $(G_4C_2)_{66}$ n=11) and lumbar spinal cord (sham n=9, $(G_4C_2)_2$ n=4, $(G_4C_2)_{66}$ n=11). One-way ANOVA analysis of the cervical spinal cord dataset was performed (p=0.2056), followed by Tukey's multiple comparisons test: sham vs. $(G_4C_2)_2$ p=0.9723, sham vs. $(G_4C_2)_{66}$ p=0.2296, $(G_4C_2)_2$ vs. $(G_4C_2)_{66}$ p=0.4228. One-way ANOVA analysis of the lumbar spinal cord dataset was performed (p=0.9341), followed by Tukey's multiple comparisons test: sham vs. $(G_4C_2)_2$ p=0.9448, sham vs. $(G_4C_2)_{66}$ p=0.9521, $(G_4C_2)_2$ vs. $(G_4C_2)_{66}$ p=0.9944, error bars = SEM.
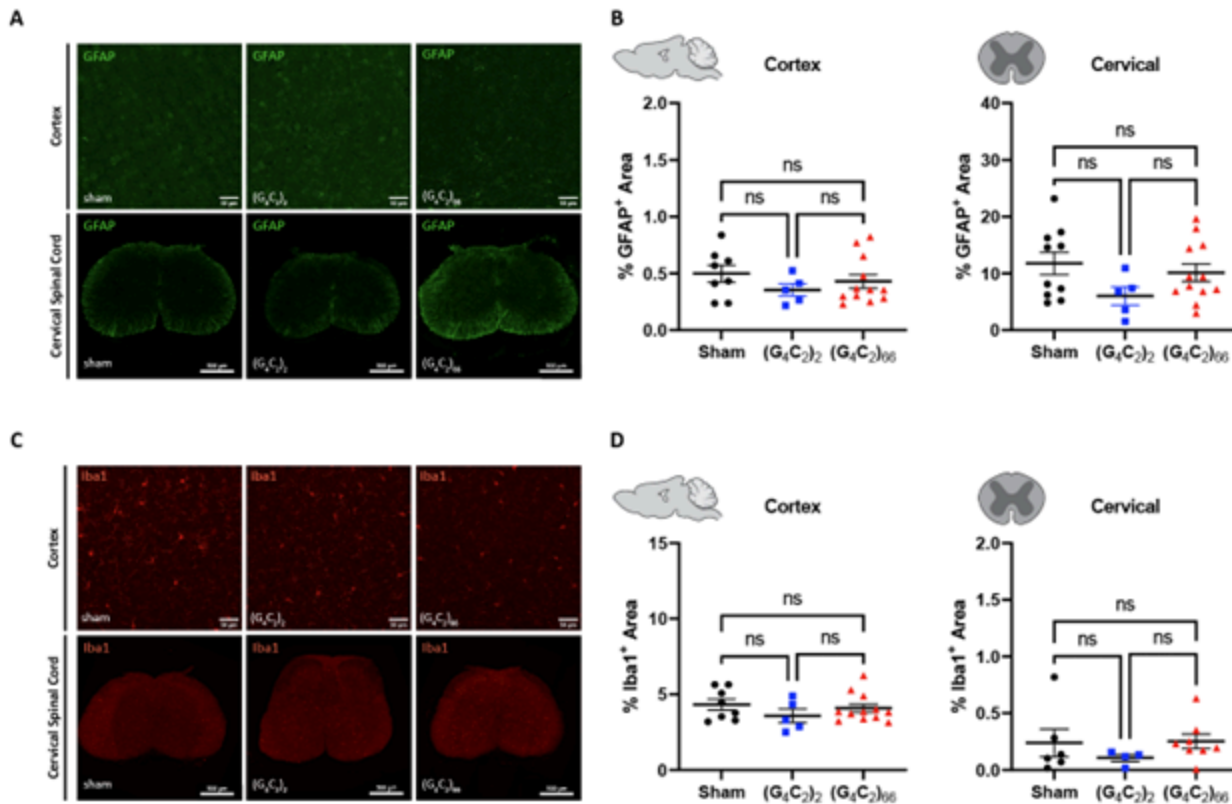
Figure 5

Analysis of gliosis in the 6-month old $(G_4C_2)_{66}$ mouse model by immunohistochemistry. **(A)** Representative images of immunohistochemistry analysis of GFAP expression within the cortex and cervical spinal cord. Cortex scale bars 50 μm and cervical spinal cord scale bars 200 μm. **(B)** Quantification of % GFAP positive area within cortex (sham n=8, $(G_4C_2)_2$ n=5, $(G_4C_2)_{66}$ n=12) and cervical spinal cord (sham n=10, $(G_4C_2)_2$ n=5, $(G_4C_2)_{66}$ n=12). One-way ANOVA analysis of the cortex dataset was performed (p=0.4382), followed by Tukey's multiple comparisons test: sham vs. $(G_4C_2)_2$ p=0.4110, sham vs. $(G_4C_2)_{66}$ p=0.7243, $(G_4C_2)_2$ vs. $(G_4C_2)_{66}$ p=0.7490. One-way ANOVA analysis of the cervical spinal cord dataset was performed (p=0.1798), followed by Tukey's multiple comparisons test: sham vs. $(G_4C_2)_2$ p=0.1558, sham vs. $(G_4C_2)_{66}$ p=0.7651, $(G_4C_2)_2$ vs. $(G_4C_2)_{66}$ p=0.3528, error bars = SEM. **(C)** Representative images of immunohistochemistry analysis of Iba1 expression within cortex and cervical spinal cord. Cortex scale bars 50 μm and cervical spinal cord scale bars 200 μm. **(D)** Quantification of % Iba1 positive area within cortex (sham n=8, $(G_4C_2)_2$ n=5, $(G_4C_2)_{66}$ n=12) and cervical spinal cord (sham n=6, $(G_4C_2)_2$ n=4, $(G_4C_2)_{66}$ n=8). One-way ANOVA analysis of the cortex dataset was performed (p=0.4234), followed by Tukey's multiple comparisons test: sham vs. $(G_4C_2)_2$ p=0.3924, sham vs. $(G_4C_2)_{66}$ p=0.8465, $(G_4C_2)_2$ vs. $(G_4C_2)_{66}$ p=0.6124. One-way ANOVA analysis of the cervical spinal cord dataset was performed (p=0.5281), followed by Tukey's multiple comparisons test: sham vs. $(G_4C_2)_2$ p=0.6173, sham vs. $(G_4C_2)_{66}$ p=0.9922, $(G_4C_2)_2$ vs. $(G_4C_2)_{66}$ p=0.5239, error bars = SEM.

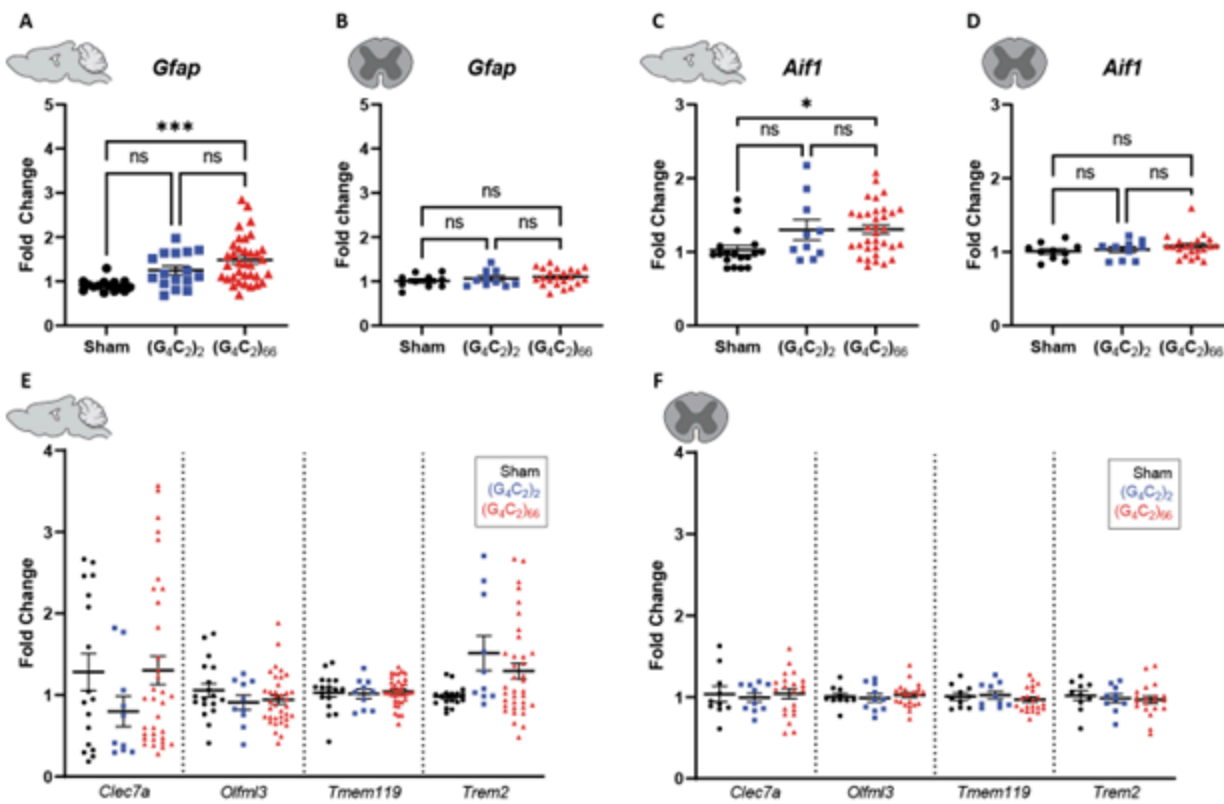**Figure 6**

Analysis of gliosis in the $(G_4C_2)_{66}$ mouse model by qRT-PCR. Analysis of *Gfap* expression within **(A)** brain (sham n=15, $(G_4C_2)_2$ n=16, $(G_4C_2)_{66}$ n=36) and **(B)** thoracic spinal cord tissue (sham n=10, $(G_4C_2)_2$ n=10, $(G_4C_2)_{66}$ n=22). Outliers were identified with the ROUT test (Q=1%) and removed from the dataset. One-way ANOVA analysis of the brain dataset was performed (p=0.0003), followed by Tukey's multiple comparisons test: sham vs. $(G_4C_2)_2$ p=0.0810, sham vs. $(G_4C_2)_{66}$ p=0.0002, $(G_4C_2)_2$ vs. $(G_4C_2)_{66}$ p=0.1774. One-way ANOVA analysis of the spinal cord dataset was performed (p=0.8903), followed by Tukey's multiple comparisons test: sham vs. $(G_4C_2)_2$ p=0.7816, sham vs. $(G_4C_2)_{66}$ p=0.3886, $(G_4C_2)_2$ vs. $(G_4C_2)_{66}$ p=0.8517. Analysis of *Aif1* expression within **(C)** brain (sham n=18, $(G_4C_2)_2$ n=10, $(G_4C_2)_{66}$ n=34) and **(D)** thoracic spinal cord tissue (sham n=10, $(G_4C_2)_2$ n=10, $(G_4C_2)_{66}$ n=21). Outliers were identified with the ROUT test (Q=1%) and removed from the dataset. One-way ANOVA analysis of the brain dataset was performed (p=0.0164), followed by Tukey's multiple comparisons test: sham vs. $(G_4C_2)_2$ p=0.1056, sham vs. $(G_4C_2)_{66}$ p=0.0156, $(G_4C_2)_2$ vs. $(G_4C_2)_{66}$ p=0.9982. One-way ANOVA analysis of the thoracic spinal cord dataset was performed (p=0.3671), followed by Tukey's multiple comparisons test: sham vs. $(G_4C_2)_2$ p=0.9225, sham vs. $(G_4C_2)_{66}$ p=0.3785, $(G_4C_2)_2$ vs. $(G_4C_2)_{66}$ p=0.6427. Analysis of *Clec7a*, *Olfml3*, *Tmem119*, and *Trem2* expression within **(E)** brain (sham n=18, $(G_4C_2)_2$ n=10, $(G_4C_2)_{66}$ n=34) and **(F)** thoracic spinal cord tissue (sham n=10, $(G_4C_2)_2$ n=10, $(G_4C_2)_{66}$ n=21). Outliers were identified with the ROUT test (Q=1%) and removed from the dataset. A one-way ANOVA was performed for each gene independently and no significant statistical difference was found in brain (*Clec7a*: p=0.3184; *Olfml3*: p=0.3836; *Tmem119*: p=0.8965; *Trem2*: p=0.1103) or spinal cord (*Clec7a*: p=0.8811; *Olfml3*: p=0.8136; *Tmem119*: p=0.5710; *Trem2*: p=0.7783) , error bars = SEM.
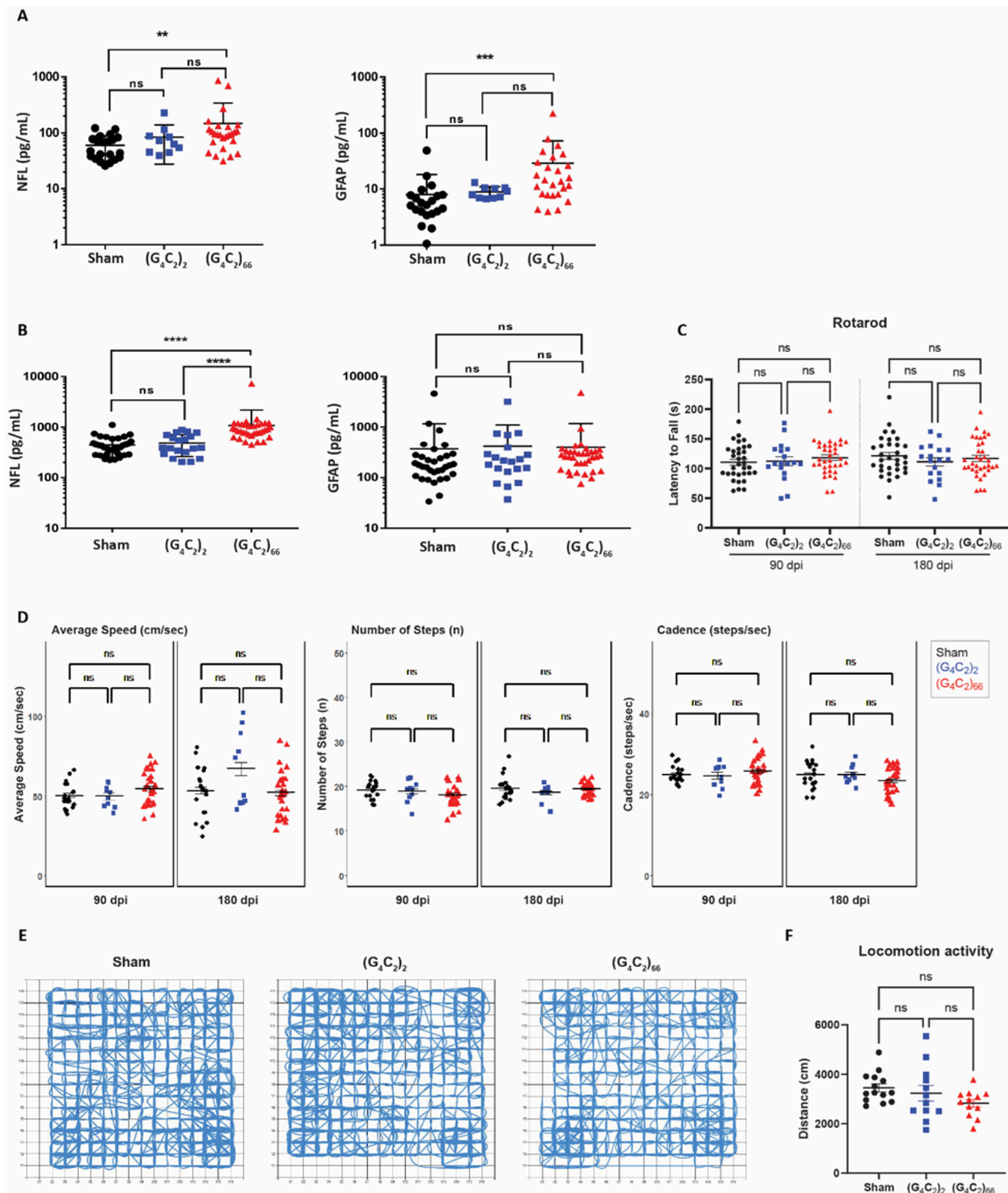
Figure 7

$(G_4C_2)_{66}$ mice do not have behavioral deficits. Analysis of NfL and GFAP levels in plasma **(A)** (sham n= 21, $(G_4C_2)_2$ n= 10, $(G_4C_2)_{66}$ n= 26). One way ANOVA followed by Dunnett's test (Dunnett, 1955). (** $p < 0.01$, *** $p < 0.001$ vs sham), and CSF **(B)** (sham n= 33, $(G_4C_2)_2$ n= 20, $(G_4C_2)_{66}$ n= 35). One way ANOVA followed by Dunnett's test. (**** $p < 0.0001$ vs sham) , error bars = SEM **(C)** Rotarod behavioral test at 90

dpi and 180 dpi (sham n=33, $(G_4C_2)_2$ n=18, $(G_4C_2)_{66}$ n=35). A repeat-measure two-way ANOVA analysis (Time: p=0.7403; Time x Group: p=0.2446; Group: 0.7403) with Sidak's multiple comparison test was performed on the dataset. 90 dpi: sham vs. $(G_4C_2)_2$ p=0.9995, sham vs. $(G_4C_2)_{66}$ p=0.7333, $(G_4C_2)_2$ vs. $(G_4C_2)_{66}$ p=0.8722; 180 dpi: sham vs. $(G_4C_2)_2$ p=0.5913, sham vs. $(G_4C_2)_{66}$ p=0.9142, $(G_4C_2)_2$ vs. $(G_4C_2)_{66}$ p=0.8827, error bars = SEM. **(D)** Catwalk behavioral test at 90 dpi and 180 dpi (sham n=20, $(G_4C_2)_2$ n=10, $(G_4C_2)_{66}$ n=27), including: average speed (cm/sec), number of steps (n), and cadence (steps/sec). Linear mixed-effects model was performed with least-squares means compared among groups and multiplicity controlled with Tukey's multiple comparisons test. Average speed: sham vs. $(G_4C_2)_2$ p=1.000 (90 dpi), p=0.9579 (180 dpi); sham vs. $(G_4C_2)_{66}$ p=0.9975 (90 dpi), p=1.000 (180 dpi); $(G_4C_2)_2$ vs. $(G_4C_2)_{66}$ p=1.000 (90 dpi), p=0.8401 (180 dpi). Number of steps: sham vs. $(G_4C_2)_2$ p=1.000 (90 dpi), p=1.000 (180 dpi); sham vs. $(G_4C_2)_{66}$ p=0.9957 (90 dpi), p=1.000 (180 dpi); $(G_4C_2)_2$ vs. $(G_4C_2)_{66}$ p=1.000 (90 dpi), p=1.000 (180 dpi). Cadence: sham vs. $(G_4C_2)_2$ p=1.000 (90 dpi), p=1.000 (180 dpi); sham vs. $(G_4C_2)_{66}$ p=1.000 (90 dpi), p=0.9997 (180 dpi); $(G_4C_2)_2$ vs. $(G_4C_2)_{66}$ p=1.000 (90 dpi), p=1.000 (180 dpi) , error bars = SEM. **(E)** Representative paths of sham, $(G_4C_2)_2$, and $(G_4C_2)_{66}$ injected mice in open-field behavioral test at 180 dpi. **(F)** Analysis of locomotion activity in the open-field test at 180 dpi (sham n=14, $(G_4C_2)_2$ n=12, $(G_4C_2)_{66}$ n=12). One-way ANOVA analysis of locomotion activity was performed (p=0.1406) followed by Tukey's multiple comparison test. sham vs $(G_4C_2)_2$ p=0.7597, sham vs $(G_4C_2)_{66}$ p=0.1219 and $(G_4C_2)_2$ vs $(G_4C_2)_{66}$ p=0.4241, error bars = SEM.

Supplementary Files

This is a list of supplementary files associated with this preprint. Click to download.

- SupplementalFigures.docx